Applied Mathematical Modelling 90 (2021) 817–844

Contents lists available at ScienceDirect

Applied Mathematical Modelling

journal homepage: www.elsevier.com/locate/apm

A novel stiffness scaling methodology for discrete element modelling of cohesive fine powders

Yi He*, Ali Hassanpour, Mohammadreza Alizadeh Behjani, Andrew E. Bayly

School of Chemical and Process Engineering, University of Leeds, Leeds LS2 9JT, UK

ARTICLE INFO

Article history:
Received 6 November 2019
Revised 6 August 2020
Accepted 22 August 2020
Available online 28 September 2020

Keywords:
DEM
van der Waals forces
Fine particles
Reduced stiffness
Packing
Additive manufacturing

ABSTRACT

The application of discrete element modelling (DEM) to cohesive fine powders in industrial processes, such as additive manufacturing, requires accurate and efficient calculations of van der Waals interaction forces. In DEM community, it is a general practice to reduce particle stiffness to accelerate the simulations; however, this study shows that, for cohesive particles, there are many cases where previously proposed scaling methodologies fail to preserve the original particle behaviour. The reason was attributed to underestimated sliding and rolling resistances and a poorly resolved non-contact cohesive interaction, thus limiting the applicability of these scaling approaches for contact-dominated systems. To address these significant issues, a new stiffness scaling methodology is proposed for the modelling of cohesive fine powders, which includes an established scaling law for contact adhesion, modified sliding and rolling resistances, and a new force-estimation scheme for the calculation of non-contact van der Waals interaction. The new approach was verified with a series of simple cases; stiffness independent results were demonstrated for head-on particle–particle collisions, particle–wall collisions, and particle-agglomerate collisions. The predictions of stop distance of a particle sliding and/or rolling over a flat surface was preserved when the stiffness was scaled down almost four orders of magnitude, which was not possible with previous scaling approaches. The new approach was further validated by packing of cohesive fine particles. This work confirmed that not only was the packing density insensitive to the particle stiffness, but the details of the packing structure (coordination number and packing density distribution) were also maintained when the original particle stiffness was scaled down by three orders of magnitude. Finally, the applicability of the new approach was explored by simulations of homogeneous simple shearing, which was found to be controlled by system cohesiveness and inertial number.

© 2020 The Author(s). Published by Elsevier Inc.
This is an open access article under the CC BY license
(http://creativecommons.org/licenses/by/4.0/)

1. Introduction

Discrete element method (DEM) has been widely used in the modelling of cohesive powders in many natural and industrial processes, such as packing [1], compaction [2–6], granular flow and fluidisation [7–10]. Particle cohesion can arise from different sources, such as van der Waals forces for fine particles [11], capillary forces for wet particles [12] and electrostatic

* Corresponding author.
E-mail addresses: Y.he1@leeds.ac.uk (Y. He), A.E.Bayly@leeds.ac.uk (A.E. Bayly).

https://doi.org/10.1016/j.apm.2020.08.062
0307-904X/© 2020 The Author(s). Published by Elsevier Inc. This is an open access article under the CC BY license
(http://creativecommons.org/licenses/by/4.0/)

forces [13], which plays an important role in the rheological behaviour of both dry [14,15] and wet cohesive granular materials [10,16,17]. A newly emerged application is additive manufacturing where fine particles are deposited in a layer-by-layer fashion to form a powder bed for selective laser sintering or electrical beam melting [18]. The presence of cohesive interaction between particles strongly affects powder behaviour during spreading and subsequently homogeneity of the deposited powder layer [19]. An accurate calculation of cohesive interaction is thus critical to achieve quantitative predictions using DEM.

DEM has been recognised as an effective tool in the study of granular materials, as it allows particles to be modelled individually and forces of various types to be explicitly considered. To model cohesive interaction between fine particles, the classic Hertzian contact theory has been extended, among which JKR [20] and DMT theories [21] are the most widely used ones. The JKR theory assumes the attractive force acts only inside contact area, resulting in a contact area larger than that of the Hertzian contact while the DMT theory assumes a Hertzian contact profile, with adhesive stress acting only outside the Hertzian contact area [8,22]. Van der Waals forces can also be directly incorporated into DEM model as an integration of forces of all pairs of atoms between two particles [1]. Van der Waals force model offers some advantages compared to the JKR and DMT theories, such as clearer physical meaning and easier implementation, and hence being the focus of this work.

In DEM modelling, an excessively small timestep is often required for typically used explicit numerical integration schemes, making it computationally very demanding for practical applications. This is especially so for modelling of cohesive fine powders. To speed up the calculations, different approaches have been proposed, including GPU computing [23,24], simplification of force models (i.e. introducing cut-off distance for long-ranged forces [25] or replacing non-linear interactions with linear ones [16]), density scaling [26] and particle size scaling [27] for quasi-static simulations. Since the critical timestep decreases with particle stiffness, adopting a reduced particle stiffness to accelerate simulations has become a common practice in DEM community. For non-cohesive particles, particle stiffness has little impact on the bulk behaviour of many systems, such as packing [28] and gas-solid fluidisation [29,30]. However, this is not the case for cohesive fine particles. Previous studies have shown that particle cohesion needs to be scaled down to compensate for the effects of a larger deformation caused by a reduced particle stiffness [29–32]. Different scaling laws have proposed for this purpose, depending on the employed contact model and adhesive force model. For example, Kobayashi et al. [29] proposed a dynamic adhesion force model for the case of constant adhesive force and linear contact model. The reduced cohesive force F_R is calculated as $F_O(k_R/k_O)^{1/2}$ with F_O being the original adhesion force, k_R and k_O the reduced and the original spring constants, respectively. Gu et al. [30] considered the van der Waals force model for both linear Hookean and Hertzian contacts, in which the reduced Hamaker constant A_R is calculated as $A_O(k_R/k_O)^{1/2}$ for the linear Hookean contact model and $A_O(Y_R/Y_O)^{2/5}$ for the Hertzian contact model, where Y represents the particle Young's modulus. For the JKR model, Hærvig et al. [33] proposed a scaling law where the surface energy density is scaled as $\gamma_R = \gamma_O(Y_R/Y_O)^{2/5}$, with γ the surface energy density. The same scaling law was also reported by Behjani et al. [34] based on a dimensionless cohesion number and Chen et al. [32] based on a dimensionless equation of motion describing particle–wall collision. Washino et al. [31] generalised this problem to different cohesive force models for both linear and non-linear contact models based on the analysis of dimensionless equation of particle motion. With the use of these scaling laws, particle sticking/rebound behaviour can be preserved. However, little attention has been paid to the sliding and rolling resistances, which are largely underestimated due to a reduced normal contact force, thus making these scaling laws only applicable for collision-dominated systems. To extend the applicability of these scaling laws to a contact-dominated system, Hærvig et al. [33] and Chen et al. [32] proposed the use of the original surface energy in the calculation of rolling and sliding resistances in the framework of JKR contact theory. However, validity and applicability of this treatment have not been properly addressed. Moreover, how to handle the calculations of sliding and rolling resistances in the framework of van der Waals force model remains unresolved.

Another important issue regarding the modelling of cohesive fine powders is the non-contact cohesive interaction. In the case of van der Waals interactions, Parteli et al. [35] pointed out that it is necessary to consider both the contact and non-contact cohesive interactions, in order to achieve a quantitative agreement with experiments on the packing of fine particles. Despite many studies have highlighted the importance of non-contact cohesive interaction [15,16,36], little attention has been paid to its calculation when using reduced particle stiffness. It is worth noting that stiffness scaling only affects contact adhesion, the presence of non-contact cohesive interaction would inevitably result in a sharp force jump when two particles just come into contact and consequently leading to large numerical errors. To avoid numerical instabilities caused by this force discontinuity (as schematically shown in Fig. 1), Gu et al. [30] proposed a modified cohesion model based on the analysis of head-on collision between two particles. The relationship between van der Waals force and particle surface separation is modified while the work done by non-contact van der Waals interaction is preserved. The modified force model works well for the fluidisation of Geldart's group A particles. However, the magnitude of non-contact van der Waals force is largely reduced, making this approach unsuitable for contact-dominated systems where interparticle force dominates the bulk behaviour. Furthermore, an enlarged DEM time step due to a reduced particle stiffness may fail to resolve the non-contact cohesive interactions, as they are only active over a short range (i.e. several nanometres for fine particles).

In view of these problems, a critical question arises: how to preserve the original particle behaviour using reduced particle stiffness while not compromising the predictive capability of DEM modelling? This study thus presents an attempt to address the issues mentioned above, namely, the underestimation of sliding and rolling resistances and the calculation of short-ranged non-contact van der Waals interaction, which are essential to achieve a stiffness-independent simulation. To

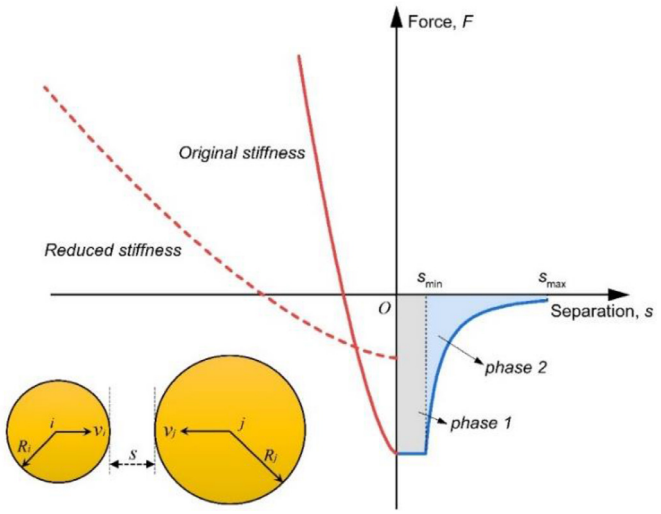

Fig. 1. Schematics of force models for both original and reduced particle properties.

this end, a systematic description, verification, validation, and applicability discussion of the proposed DEM approach are covered. The rest of the paper is structured as follows: Section 2 details the methodology for stiffness scaling by deriving dimensionless equations of motion, which includes a scaling law for contact adhesion, modified sliding and rolling resistances, and a prediction-correction scheme for the calculation of non-contact cohesive interaction. In Section 3, the proposed method is first examined through a series of simple verification tests, including head-on collisions between two particles and particle sliding and/or rolling along a flat surface. The performance is then evaluated and confirmed by the packing of fine particles. Finally, the applicability of this approach is explored by simulations of homogeneous simple shearing over a range of controlled pressures.

2. Model development

2.1. DEM and force models

In DEM modelling, translational and rotational motions of all particles are governed by Newton's second law of motion. For fine particles, an additional van der Waals force must be considered. The resulting governing equations can be written as,

$$m_i \frac{d\mathbf{v}_i}{dt} = \sum_j \left(\mathbf{F}_{n,ij} + \mathbf{F}_{t,ij}\right) + \sum_k \mathbf{F}_{v,ik} + m_i\mathbf{g} \tag{1}$$

$$I_i \frac{d\omega_i}{dt} = \sum_j \left(\mathbf{T}_{t,\,ij} + \mathbf{T}_{r,\,ij}\right) \tag{2}$$

where m_i is the mass, I_i is the moment of inertia, $\mathbf{v}_i$ and $\boldsymbol{\omega}_i$ are the translational and rotational velocities of particle i, respectively. The forces acting on each particle can be decomposed into normal and tangential components, $\mathbf{F}_{n,ij}$ and $\mathbf{F}_{t,ij}$, due to the collision with other particles or walls, long-ranged force due to van der Waals interaction $\mathbf{F}_{v,ik}$ and body force due to gravity, $m_i\mathbf{g}$. The torques involve $\mathbf{T}_{t,\,ij}$ due to the tangential contact force,

$$\mathbf{T}_{t,ij} = \mathbf{r}_{ij} \times \mathbf{F}_{t,ij} \tag{3}$$

with $\mathbf{r}_{ij}$ a vector pointing from the centre of particle i to the contact point between particle i and j, and $\mathbf{T}_{r,\,ij}$ accounting for the rotational resistance,

$$\mathbf{T}_{r,ij} = \mu_r \left|\mathbf{F}_{cn,ij}\right| \boldsymbol{\omega}_i / |\boldsymbol{\omega}_i| \tag{4}$$

due to the asymmetric distribution of the contact pressure, with μ_r the rolling friction coefficient and $\mathbf{F}_{cn,ij}$ the normal contact force. The normal contact force is described by the Hertzian contact theory while the tangential contact force is based on the Mindlin and Deresiewicz theory [37].

Particle collision in DEM is handled by a so-called soft-sphere model, thereby allowing for a small overlap to be formed between two contacted particles. Based on the magnitude of the overlap δ_n, normal force between particle i and j, $\mathbf{F}_{n,ij}$, can

be determined as,

$$\mathbf{F}_{n,ij} = \frac{4}{3}E^* R^{*1/2}\delta_n^{3/2}\hat{\mathbf{n}} + 2\sqrt{\frac{5}{6}}\beta_n\sqrt{S_n m^*}\mathbf{v}_{ij}^n \tag{5}$$

where the effective radius R^* is given by $R^* = R_i R_j/(R_i + R_j)$, $m^* = m_i m_j/(m_i + m_j)$ is the reduced mass and $\hat{\mathbf{n}}$ is the unit normal vector. The first term in Eq. (5) is the normal contact force, $\mathbf{F}_{cn,ij}$, due to elastic deformation described as a Hertzian elastic contact, in which the effective elastic modulus E^* is calculated as,

$$\frac{1}{E^*} = \frac{\left(1-\nu_i^2\right)}{Y_i} + \frac{\left(1-\nu_j^2\right)}{Y_j} \tag{6}$$

with Y_i being the Young's modulus and ν_i the Poisson's ratio of particle i. The second term in Eq. (5) is the normal damping force, $\mathbf{F}_{dn,ij}$, which is responsible for the energy dissipation due to viscous damping, with $S_n = 2E^*\sqrt{R^*\delta_n}$. For collision between two non-cohesive particles, the normal damping coefficient β_n can be linked to the restitution coefficient of normal collision e_n (defined as the ratio of post-collisional contact velocity to pre-collisional contact velocity) [38,39] and is given as,

$$\beta_n = \frac{\ln(e_n)}{\sqrt{\pi^2 + \ln^2(e_n)}} \tag{7}$$

However, for cohesive particles, the resulting restitution coefficient depends on the collision velocities and there exists a critical impact velocity below which two particles would stick together. The resulting restitution coefficient approaches e_n with increasing impact velocities.

The tangential force ($\mathbf{F}_{t,ij}$) is also composed of a contact force ($\mathbf{F}_{ct,ij}$) and a damping force ($\mathbf{F}_{dt,ij}$). The tangential contact force is based on the Mindlin and Deresiewicz theory [37] and is given as,

$$\mathbf{F}_{ct,ij} = \begin{cases} -\mu_t\left|\mathbf{F}_{cn,ij}\right|\left[1-\left(1-\left|\boldsymbol{\delta}_t\right|/\delta_{t,\max}\right)^{3/2}\right]\hat{\boldsymbol{\delta}}_t + \mathbf{F}_{dt,ij} & \left|\boldsymbol{\delta}_t\right| < \delta_{t,\max} \\ -\mu_t\left|\mathbf{F}_{cn,ij}\right|\hat{\mathbf{v}}_t & \left|\boldsymbol{\delta}_t\right| \geq \delta_{t,\max} \end{cases} \tag{8}$$

where μ_t is the Coulomb friction coefficient. $\boldsymbol{\delta}_t$ represents particle displacement in the tangential direction and $\hat{\boldsymbol{\delta}}_t = \delta_t/|\delta_t|$, while $\hat{\mathbf{v}}_t = \mathbf{v}_t/|\mathbf{v}_t|$ is the unit vector of the relative velocity in the tangential direction. Here, $\delta_{t,\max} = \mu_t\delta_n(2-\nu)/(2-2\nu)$ is the critical tangential displacement, which distinguishes the friction state as static friction or dynamic sliding friction. The tangential damping force is given as,

$$\mathbf{F}_{dt,ij} = 2\sqrt{\frac{5}{6}}\beta_t\sqrt{S_t m^*}\mathbf{v}_{ij}^t \tag{9}$$

in which β_t is the tangential damping coefficient which can also be determined by Eq. (7) and $\mathbf{v}_{ij}^t$ is the relative velocity in the tangential direction. $S_t = 8G^*\sqrt{R^*\delta_n}$, with G^* the effective shear modulus and calculated as,

$$\frac{1}{G^*} = \frac{2(2-\nu_i)(1+\nu_i)}{Y_i} + \frac{2\left(2-\nu_j\right)\left(1+\nu_j\right)}{Y_j} \tag{10}$$

For fine powders, the van der Waals force between two spherical particles is estimated based on the Hamaker theory [11],

$$\mathbf{F}_{v,ik} = \begin{cases} \frac{AR^*}{6s_{\min}^2}\hat{\mathbf{n}} & s < s_{\min} \\ \frac{AR^*}{6s^2}\hat{\mathbf{n}} & s_{\min} \leq s \leq s_{\max} \\ 0 & s \geq s_{\max} \end{cases} \tag{11}$$

where s is the interparticle separation distance,

$$s = |\mathbf{r}_i - \mathbf{r}_k| - (R_i + R_k) \tag{12}$$

and A is the Hamaker constant, which is material-specific and can be related to the surface energy γ by the following equation [35],

$$A = 24\pi s_{\min}^2\gamma \tag{13}$$

The van der Waals force is assumed to be constant when the surface separation between two particles is smaller than a minimum separation $s_{\min}$ which is a cut-off distance introduced to avoid the singularity when the surface separation equals to zero. A maximum cut-off distance $s_{\max}$ is also introduced because the magnitude of van der Waals force drops dramatically with increasing separation. Fig. 1 schematically shows the van der Waals force as a function of particle separation, where the van der Waals interaction can be divided into two parts: contact and non-contact cohesive interactions.

2.2. Dimensionless governing equations of motion

In soft-sphere DEM model, a reduced particle stiffness allows a larger overlap to be formed between two contacted particles. It is thus necessary to scale down the van der Waals interaction for cohesive fine particles; otherwise more kinetic energy would be consumed due to an enlarged overlap. Such a scaling law can be obtained from the dimensionless equations of motion. The idea is that the original contact behaviour can be preserved if the dimensionless equation of motion does not change over stiffness scaling. In the following, dimensionless equations of motion are presented for both the normal and tangential interactions. Noting that non-contact van der Waals interaction is not considered here.

In the normal direction, we consider a collision between two particles with an initial relative velocity of $v_{n,0}$, the governing equation of motion can be written as,

$$m\frac{d|\mathbf{v}_n|}{dt} = |\mathbf{F}_{cn}| + |\mathbf{F}_{dn}| - |\mathbf{F}_v| \tag{14}$$

where $\mathbf{v}_n$ is the particle velocity in the normal direction. A characteristic contact overlap can be introduced from the perspective of energy conservation, i.e.,

$$\int_0^{\delta_c} |\mathbf{F}_{cn}| d\delta_n = \frac{8}{15} E\sqrt{R}\delta_c^{5/2} = \frac{1}{2} m v_{n,0}^2 \tag{15}$$

The normal overlap can thus be scaled with δ_m, given as,

$$\delta_m = \left(\frac{m v_{n,0}^2}{E\sqrt{R}}\right)^{2/5} = \left(\frac{K}{L}\right)^{2/5} \tag{16}$$

in which $K = m v_{n,0}^2$ and $L = E\sqrt{R}$. The resulting dimensionless normal velocity, $\hat{v}_n$, and dimensionless normal overlap, $\hat{\delta}_n$, can thus be written as,

$$\hat{v}_n = \frac{|\mathbf{v}_n|}{v_{n,0}} \tag{17}$$

$$\hat{\delta}_n = \delta_n \left(\frac{L}{K}\right)^{2/5} \tag{18}$$

The dimensionless governing equation of motion can be obtained by substituting Eqs. (17) and (18) into Eq. (14). For the inertial force term,

$$m\frac{d|\mathbf{v}_n|}{dt} = m\frac{d|\mathbf{v}_n|}{d\delta_n}\frac{d\delta_n}{dt} = m|\mathbf{v}_n|\frac{d|\mathbf{v}_n|}{d\delta_n} = K^{3/5}L^{2/5}\hat{v}_n\frac{d\hat{v}_n}{d\hat{\delta}_n} \tag{19}$$

For the normal contact force,

$$|\mathbf{F}_{cn}| = c_0 E\sqrt{R}\delta_n^{3/2} = c_0 K^{3/5}L^{2/5}\hat{\delta}_n^{3/2} \tag{20}$$

where $c_0 = 4/3$ is the constant. For the normal damping force,

$$|\mathbf{F}_{dn}| = c_1 m^{1/2}\left(E\sqrt{R}\right)^{1/2}\delta_n^{1/4}|\mathbf{v}_n| = c_1 K^{3/5}L^{2/5}\hat{\delta}_n^{1/4}\hat{v}_n \tag{21}$$

where $c_1 = \sqrt{20/3}\beta$ is the constant. For van der Waals force during contact,

$$|\mathbf{F}_v| = \frac{AR}{6s_{\min}^2} = c_2 RA \tag{22}$$

In which $c_2 = 1/6s_{\min}^2$ is the constant. The resulting dimensionless equation of motion in the normal direction can be written as,

$$\hat{v}_n\frac{d\hat{v}_n}{d\hat{\delta}_n} - c_0\hat{\delta}_n^{3/2} - c_1\hat{\delta}_n^{1/4}\hat{v}_n + c_2 RK^{-3/5}L^{-2/5}A = 0 \tag{23}$$

In the tangential direction, we consider a collision with an initial relative tangential velocity of $v_{t,0}$. In the dynamic frictional regime, the governing equation of motion is written as,

$$m\frac{d|\mathbf{v}_t|}{dt} = \mu_t|\mathbf{F}_{cn}| \tag{24}$$

The time can be scaled with t_m,

$$t_m = \frac{\delta_m}{v_{n,0}} = \left(\frac{K}{L}\right)^{2/5} v_{n,0}^{-1} \tag{25}$$

The dimensionless tangential velocity, $\hat{v}_t$, and the dimensionless time can be calculated as,

$$\hat{v}_t = \frac{|\mathbf{v}_t|}{v_{t,0}} \tag{26}$$

$$\hat{t} = \frac{t}{t_m} \tag{27}$$

The resulting dimensionless form of the governing equation is,

$$\left(\frac{T}{K}\right)^{1/2}\frac{d\hat{v}}{d\hat{t}} - \mu c_0 \hat{\delta}_n^{3/2} = 0 \tag{28}$$

where $T = mv_{t,0}^2$.

The governing equation of motion in the regime of static friction can be written as,

$$m\frac{d|\mathbf{v}_t|}{dt} = \mu_t |\mathbf{F}_{cn}|\left[1 - \left(1 - |\boldsymbol{\delta}_t|/\delta_{t,\max}\right)^{3/2}\right] + |\mathbf{F}_{dt}| \tag{29}$$

The dimensionless tangential velocity, $\hat{v}_t$, and tangential displacement, $\hat{\delta}_t$, can be calculated as,

$$\hat{v}_t = \frac{|\mathbf{v}_t|}{v_{t,0}} \tag{30}$$

$$\hat{\delta}_t = \frac{|\boldsymbol{\delta}_t|}{\delta_{t,\max}} \tag{31}$$

in which $\delta_{t,\max} = \mu_t\delta_n(2-\nu)/(2-2\nu)$. For the inertial force term,

$$m\frac{d|\mathbf{v}_t|}{dt} = mv_{t,0}\frac{d\hat{v}_t}{d\delta_t}\frac{d\delta_t}{dt} = mv_{t,0}^2\frac{d\hat{v}_t}{c_3\delta_n d\hat{\delta}_t}\hat{v}_t = c_4 T\left(\frac{L}{K}\right)^{2/5}\frac{d\hat{v}_t}{\hat{\delta}_n d\hat{\delta}_t}\hat{v}_t \tag{32}$$

where $c_3 = \mu_t(2-\nu)/(2-2\nu)$ and $c_4 = 1/c_3$ are constants. For the static frictional force,

$$\mu|\mathbf{F}_{cn}|\left[1 - \left(1 - |\boldsymbol{\delta}_t|/\delta_{t,\max}\right)^{3/2}\right] = \mu c_0 K^{3/5}L^{2/5}\hat{\delta}_n^{3/2}\left[1 - \left(1-\hat{\delta}_t\right)^{3/2}\right] \tag{33}$$

For the tangential damping force,

$$|\mathbf{F}_{dt}| = 2\sqrt{\frac{5}{6}}\beta_t\sqrt{S_t m^*}|\mathbf{v}_t| = c_5 K^{1/10}L^{2/5}T^{1/2}\hat{\delta}_n^{1/4}\hat{v}_t \tag{34}$$

in which $c_5 = 4\sqrt{\frac{5}{6}}(\frac{1-\nu_i}{2-\nu_i})^{1/2}$is a constant. For the regime of static friction, the dimensionless form of the governing equation can then be written as,

$$c_4\frac{d\hat{v}_t}{d\hat{\delta}_t}\hat{v}_t - \mu c_0\left(\frac{K}{T}\right)\hat{\delta}_n^{5/2}\left[1 - \left(1-\hat{\delta}_t\right)^{3/2}\right] - c_5\left(\frac{K}{T}\right)^{1/2}\hat{\delta}_n^{5/4}\hat{v} = 0 \tag{35}$$

Similarly, a dimensionless rotational velocity, $\hat{\omega}$, can be calculated by scaling with initial rotational velocity ω_0 as,

$$\hat{\omega} = \frac{|\boldsymbol{\omega}|}{\omega_0} \tag{36}$$

with ω_0 the initial rotational velocity. The resulting dimensionless equation of rotational motion is,

$$I\omega_0 v_{n,0}K^{-1}\frac{d\hat{\omega}}{d\hat{t}} - \mu_r c_0\hat{\delta}_n^{3/2} = 0 \tag{37}$$

2.3. A scaling law for contact adhesion

To maintain collision outcome, the dimensionless governing equations of motion (i.e. Eqs. (23), (28), (33), (35) and (37)) should be kept the same for particles of different stiffnesses. To be more specific, in the normal direction, the fourth term $c_2RK^{-3/5}L^{-2/5}A$ in Eq. (23) should be preserved over stiffness scaling. The following scaling law can then be obtained,

$$\frac{A^R}{A^O} = \left(\frac{E^R}{E^O}\right)^{2/5} = \left(\frac{Y^R}{Y^O}\right)^{2/5} = \chi^{2/5} \tag{38}$$

where the superscripts R refers to reduced particle properties while O refers to the original particle properties. $\chi = Y^R/Y^O$ is the scaling ratio of particle Young's modulus. Same scaling law was also reported by Gu et al. [30] and Washino et al. [31].

It is worth noting that the dimensionless equations for sliding and rolling motions are independent on particle stiffness, as shown by Eqs. (28), (33), (35) and (37). In the absence of non-contact cohesive interaction, this scaling law (i.e. Eq. (38)) alone is thus able to preserve the collision outcome over stiffness scaling.

2.4. A modified sliding and rolling resistances

As shown before, the scaling law (i.e. Eq. (38)) is expected to work well for a collision-dominated system, as bulk behaviour is mainly determined by collision outcome between particles. However, this is not the case for a contact-dominated system, as the sliding and rolling resistances are largely under-predicted due to a reduced normal contact force (i.e. $|\mathbf{F}_{cn}^{R}| < |\mathbf{F}_{cn}^{O}|$). In other words, despite post-collisional tangential and rotational velocities are not affected by stiffness scaling, the sliding and rotational displacements are over-predicted due to an enlarged contact period of a softer particle. It is thus necessary to estimate the magnitude of original normal contact force to be used in the calculations of sliding and rolling resistances.

Considering a contact-dominated system under a given pressure P, the typical contact force in the system is of order Pd^2, with d the particle diameter. At each contact, the following force balance is valid for both original and reduced particle properties at steady state,

$$Pd^2 + |\mathbf{F}_v| = |\mathbf{F}_{cn}| \tag{39}$$

Take the tangential contact force as an example,

$$F_{ct} = \mu_t \left|\mathbf{F}_{cn}^{O}\right| = \mu_t \left(Pd^2 + \left|\mathbf{F}_{v}^{O}\right|\right) = \mu_t \left(\left|\mathbf{F}_{cn}^{R}\right| - \left|\mathbf{F}_{v}^{R}\right| + \left|\mathbf{F}_{v}^{O}\right|\right) \tag{40}$$

The normal contact force, $\mathbf{F}_{cn,ij}$, used in the calculations of sliding and rolling resistances (i.e. Eqs. (4) and (8)) can thus be replaced with a modified normal contact force $\mathbf{F}_{cn,\,ij}^{M}$, given as,

$$\left|\mathbf{F}_{cn,ij}^{\mathrm{M}}\right| = \left|\mathbf{F}_{cn,ij}\right| - \left|\mathbf{F}_{v,ij}\right| + \left|\mathbf{F}_{v,ij}^{O}\right| \tag{41}$$

where the $|\mathbf{F}_{cn,ij}|$ and $|\mathbf{F}_{v,ij}|$ are calculated by a reduced particle stiffness. The underlying assumption of this modification is that transient response of normal contact force has little impact on the bulk behaviour. This is indeed valid for systems dominated by enduring contacts, as transient behaviour dies out quickly due to damping. Once the steady normal contact force matches, particle stiffness shows very little effect on the bulk behaviour. This is also evidenced in the systems consisting of non-cohesive particles, where the contact pressure is dominated by the external pressure. Despite softer particle takes longer to reach steady state, the resulting bulk behaviour is not much affected.

2.5. A force-estimation scheme for non-contact cohesive interaction

In conventional DEM approach, the magnitudes of interparticle forces are estimated based on the relative position between two particles. That is, within one timestep, these forces are regarded as constant. For the explicit numerical integration schemes typically used in DEM calculation, the time step must be sufficiently small to resolve the collision event. For the Hertzian contact model, collision time for two spheres with same material and diameter can be calculated as [29],

$$t_{\mathrm{col}} = 2.943\left(\frac{5\sqrt{2}\pi\,\rho\left(1-\nu^2\right)}{4Y}\right)^{2/5}\frac{R}{v_0^{1/5}} \tag{42}$$

with v_0 being the approaching velocity before two particles come into contact. Normally, the DEM time step can be estimated as,

$$\Delta t_{\mathrm{DEM}} = \alpha \cdot t_{\mathrm{col}} \tag{43}$$

with the factor α being around 0.02 (i.e. 50 steps). However, previous studies showed that DEM timestep is further limited if attractive forces are present [31], namely, the time step determined by Eq. (43) may not be small enough to resolve van der Waals interaction when two particles are not in contact. This is especially the case when using a reduced particle stiffness to resolve the collision.

To overcome this additional constraint on timestep and the force discontinuity induced by reduced particle stiffness (as schematically shown in Fig. 1), we proposed a new prediction-correction scheme for the calculation of non-contact cohesive interaction. The van der Waals interaction is differentiated into two parts: a contact adhesion and a non-contact cohesive interaction. The contact adhesion is resolved using the conventional DEM approach (i.e. the force magnitude is estimated based on the relative position between two particles), which results in a prediction of particle's position and velocity. The work done by non-contact cohesive interaction (if present) can then be calculated based on the predicted particle position, which can then be used to correct particle velocity. To be compatible with the soft-sphere DEM model, an impulse is estimated from the corrected particle velocity, yielding an effective cohesive force. By doing so, a solution insensitive to the time step can be obtained when using a reduced particle stiffness. It should be noted that this approach is able to preserve the maximum adhesive force, active range and work done by the van der Waals force, but at a cost of reduced accuracy in the calculation of particle position. However, due to the small active range of non-contact van der Waals interaction (i.e. several nanometres for fine particles), this reduced accuracy does not affect much of the collision behaviour, as shown later in the verification tests. In fact, previous studies showed that functional form of the non-contact cohesive model has little influence on the steady-state rheology, such as flow structure [36], steady-state cohesion [16] and volume fraction of sheared materials [15]. In particular, Roy et al. [16] pointed out that as long as the maximum adhesive

force and total energy dissipation per contact are matched, the non-linear cohesive model can be simplified into a linear model. In the following sections, analytical solutions of the corrected particle velocity are derived for both particle–particle and particle–wall interactions.

2.5.1. Particle–particle interaction

Considering two particles located in the proximity of each other, non-contact van der Waals force acts only in a direction pointing from the centre of one particle to another. Depending on the relative velocity, it can either promote or restrict the motion of the particle. Changes in particle velocity due to this non-contact cohesive interaction can be calculated by enforcing momentum and energy conservations for the two particles, i.e.,

$$m_i v_{i,n} + m_j v_{j,n} = M \tag{44}$$

$$m_i v_{i,n}^2 + m_j v_{j,n}^2 = N \tag{45}$$

in which,

$$M = m_i v_{i0,n} + m_j v_{j0,n} \tag{46}$$

$$N = 2W + m_i v_{i0,n}^2 + m_j v_{j0,n}^2 \tag{47}$$

where $v_{i0,n}$ and $v_{j0,n}$ are the particle velocities in the normal direction before the van der Waals interaction taking effect and $v_{i,n}$ and $v_{j,n}$ are the velocities after that. W is the work done by van der Waals force. Rearranging and substituting Eq. (44) into Eq. (45) results in the following equation of $v_{j,n}$,

$$\frac{M^2 + \left(m_j v_{j,n}\right)^2 - 2M m_j v_{j,n}}{m_i} + m_j v_{j,n}^2 = N \tag{48}$$

Solving the above equations, the resulting velocity $v_{j,n}$ is,

$$v_{j,n} = \frac{2Mm_j \pm \sqrt{\left(2Mm_j\right)^2 - 4\left(M^2 - Nm_i\right)\left(m_i m_j + m_j^2\right)}}{2\left(m_i m_j + m_j^2\right)} \tag{49}$$

Here, we introduce a critical velocity $v_{crit,n}$ at which two particles will stick to each other after cohesive interaction as,

$$v_{crit,n} = \frac{M}{\left(m_i + m_j\right)} \tag{50}$$

We assume the velocity change is small so that the sign of velocity relative to the critical velocity remains unchanged after the cohesive interaction. Therefore,

$$v_{j,n} = \begin{cases} \dfrac{2Mm_j + \sqrt{\left(2Mm_j\right)^2 - 4\left(M^2 - Nm_i\right)\left(m_i m_j + m_j^2\right)}}{2\left(m_i m_j + m_j^2\right)} & \text{if } v_{j,n} \geq v_{crit,n} \\ \dfrac{2Mm_j - \sqrt{\left(2Mm_j\right)^2 - 4\left(M^2 - Nm_i\right)\left(m_i m_j + m_j^2\right)}}{2\left(m_i m_j + m_j^2\right)} & \text{if } v_{j,n} < v_{crit,n} \end{cases} \tag{51}$$

To calculate the work due to cohesive interaction, it is necessary to differentiate the mode of relative motion as, i) two particle are approaching each other and ii) two particles are moving apart from each other. For each type of relative motion, the work due to cohesive interaction is calculated separately. For the first mode of relative motion, the predicted surface separation $s'_{t+\Delta t}$(without considering the effect of non-contact van der Waals force) is smaller than s_t (the surface separation at the current time step) and $s_t > 0$. The positive work arising from the cohesive interaction can be calculated as,

$$W = \begin{cases} W_1 = \dfrac{(s_t - s_{pt})AR^*}{6s_{min}^2} & \text{if } s_t < s_{min} \\ W_2 & \text{if } s_t \geq s_{min} \end{cases} \tag{52}$$

in which,

$$W_2 = \begin{cases} \dfrac{AR^*}{6s_{pt}} - \dfrac{AR^*}{6s_t} & s_{pt} > s_{min} \\ \dfrac{(s_{min} - s_{pt})AR^*}{6s_{min}^2} + \dfrac{AR^*}{6}\left(\dfrac{1}{s_{min}} - \dfrac{1}{s_t}\right) & s_{pt} \leq s_{min} \end{cases} \tag{53}$$

where $s_{pt} = \max(0,\ s'_{t+\Delta t}\ )$

When two particle are separating from each other, as determined by the condition that $s'_{t+\Delta t} > s_t$ and $s'_{t+\Delta t} > 0$, the negative work due to the cohesive interaction can be calculated by the following equations,

$$W = \begin{cases} W_3 & \text{if } s'_t < s_{\min} \\ W_4 = \frac{AR^*}{6}\left(\frac{1}{s'_{t+\Delta t}} - \frac{1}{s'_t}\right) & \text{if } s'_t \geq s_{\min} \end{cases} \tag{54}$$

in which,

$$W_3 = \begin{cases} \frac{\left(s'_t - s_{\min}\right)AR^*}{6s_{\min}^2} + \frac{AR^*}{6}\left(\frac{1}{s'_{t+\Delta t}} - \frac{1}{s_{\min}}\right) & s'_{t+\Delta t} > s_{\min} \\ \frac{\left(s'_t - s'_{t+\Delta t}\right)AR^*}{6s_{\min}^2} & s'_{t+\Delta t} \leq s_{\min} \end{cases} \tag{55}$$

where $s'_t = \max(0,\ s_t\ )$.

2.5.2. Particle–wall interaction

For particle–wall interaction, since the mass of wall is significantly larger than individual particles, velocity change of wall due to non-contact van der Waals interaction can thus be reasonably ignored. Eqs. (44) and (45) can then be reduced to the following,

$$m_i v_{i,n}^2 = M = 2W + m_i v_{i0,n}^2 \tag{56}$$

Accordingly, the corrected particle velocity due to the particle–wall cohesive interaction is calculated as,

$$v_{i,n} = \begin{cases} W_5 & \text{if } M > 0 \\ v_{\text{wall},n} & \text{if } M = 0 \end{cases} \tag{57}$$

in which,

$$W_5 = \begin{cases} \sqrt{M/m_i} & \text{if } v_{i,n} > v_{\text{wall},n} \\ -\sqrt{M/m_i} & \text{if } v_{i,n} \leq v_{\text{wall},n} \end{cases} \tag{58}$$

2.5.3. Effective non-contact van der Waals force

The velocity correction due to non-contact van der Waals interaction can be incorporated into the soft-sphere DEM model by estimating the impulse acting on the particle during one DEM time step. This translational velocity change due to the cohesive interaction can be converted to a force by dividing the time step used for DEM simulation. For particle *i*, the modified van der Waals force is given by,

$$\mathbf{F}_{v,i} = \sum_k \frac{m_i(v_{i,n} - v_{i0,n})\hat{\mathbf{n}}_{ik}}{\Delta t_{\text{DEM}}} \tag{59}$$

where the summation runs over all the neighbouring particles of the given particle *i*.

3. Results and discussion

The developed DEM approach is systematically evaluated via a series of verification cases and is validated by the packing of fine particles, where comparisons between reduced and original particle stiffnesses are made. Specifically, head-on collisions between two particles, oblique particle–wall collisions (see Appendix A.1) and particle-agglomerate collisions (see Appendix A.2) are conducted to verify the proposed prediction-correction scheme. The calculations of sliding and rolling resistances is examined by modelling a particle sliding and/or rolling on a flat surface. The distance that particle travels before friction brings to a stop is recorded and compared with the existing scaling approach. The performance of the present DEM approach in dense particulate systems is demonstrated by simulations of fine particles packing with and without accounting for the non-contact van der Waals interaction. Three particle sizes are tested, and comparisons are made against the typically used conventional DEM approach (i.e. force magnitude is estimated based on the relative position between two particles) in terms of both global packing density and detailed packing structure. Finally, applicable range of this approach is evaluated by simulations of homogeneous simple shearing over a range of controlled pressures, with a focus on the prediction of steady-state volume fraction and stress ratio.

3.1. Model verification

3.1.1. Head-on collision between two particles

A series of head-on collisions between two particles are carried out to verify the proposed force-estimation scheme. An effective restitution coefficient (e_{eff}) is defined as the ratio of velocities before and after a collision. It should be noted that,

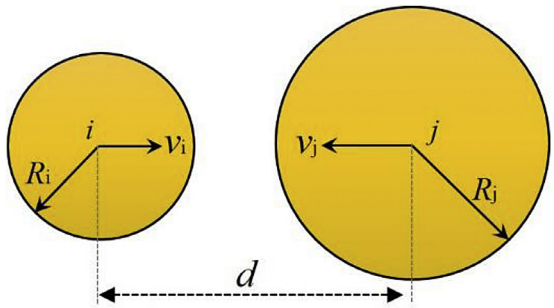

Fig. 2. The schematic of head-on collisions between two particles, where initial distance between the two particles is set to 1.2 times of the sum of two particles' radii.

Table 1
Parameters used in the simulations of two particle collision.

Parameter	Value
Particle diameter, d_p (μm)	120
Particle density, ρ (kg/m^3)	2250
Poisson's ratio, ν	0.22
Sliding friction coefficient, μ_s	0.3
Rolling friction coefficient, μ_r	0.02
Normal restitution coefficient, e_n	0.3, 0.6, 0.94
Hamaker constant, A (J)	4.2×10^{-20}
Minimum cut-off distance, s_{min} (nm)	1.0
Maximum cut-off distance, s_{max}	$d_p/8$

Table 2
Particle Young's modulus tested and its corresponding Bond number (Bo_c).

Young's modulus (Pa)	7×10^{10}	10^8	10^6
Contact Bond number, Bo_c	3.97×10^{-10}	2.78×10^{-7}	2.78×10^{-5}

for cohesive powders, e_{eff} is different from but gradually reaches e_n (as shown in Eq. (7)) with increasing impact velocity. There also exists a critical impact velocity below which the two particles remain stuck together (i.e. $e_{eff} = 0$).

As schematically shown in Fig. 2, the initial distance between two particles is set to 1.2 times of the sum of the two particles' radii to enable the non-contact van der Waals interaction. A range of impact velocities are tested so that a relationship between the effective restitution coefficient (e_{eff}) and impact velocity can be established. The present model is solved numerically using an explicit time integration method with a fixed time step determined by Eqs. (42) and (43). Table 1 summaries the parameters used in the simulation. Particle gravity is not considered while particle Young's modulus is varied here. A contact Bond number, Bo_c, is introduced to quantify the cohesive strength, which is defined as the ratio of the maximum adhesive force to a characteristic contact force (i.e. $Bo_c = |\mathbf{F}_v^{max}|/(E^* d^2)$, with E^* the effective elastic modulus calculated by Eq. (6)) [40]. The tested particle Young's modulus and the corresponding contact Bond number are listed in Table 2.

Head-on collisions are first simulated using initial velocities of equal magnitude but opposite directions. The two particles have same size and consequently the post-collisional velocities are equal in magnitude. Fig. 3(a) shows the results obtained using a particle Young's modulus of 7×10^{10} Pa. A slightly decrease in the effective restitution coefficient can be observed at small velocities if only accounting for the contact adhesion. In contrast, with the presence of the non-contact van der Waals interaction, there exists a critical impact velocity around 1.1×10^{-4} m/s below which particles stick together. The effective restitution coefficient shows a sharp increase when impact velocity is slightly larger than the critical impact velocity and gradually approaches e_n with further increase of the impact velocity. The presence of non-contact van der Waals interaction shows a significant impact on the collision behaviour, suggesting the necessity to consider it in simulations of fine particles.

Contrary to that of non-cohesive particles, particle stiffness shows an influence on the collision outcome of cohesive fine particles. Fig. 3(b) shows the effect of particle stiffness on the relationship between effective restitution coefficient and impact velocity, where the critical impact velocity increases with the decrease of particle Young's modulus. The reason can be attributed to a larger overlap that can be formed between two softer particles, consequently leading to a larger dissipation of kinetic energy by the van der Waals interaction and hence a larger critical impact velocity. Fig. 3(c) shows the performance of previously proposed scaling law if non-contact van der Waals interaction is present. Compared to the results of original particle stiffness, a strong scattering of the effective restitution coefficient can be observed when the particle Young's modulus is reduced to 10^{-6}, although a scaled Hamaker constant is used in the calculation of contact adhesion (i.e. for $s < s_{min}$ in Eq. (11)). The discrepancy can be attributed to the force discontinuity observed at zero surface separation

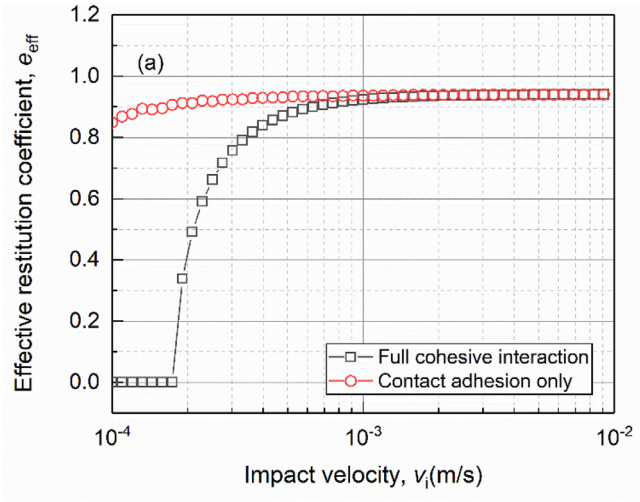

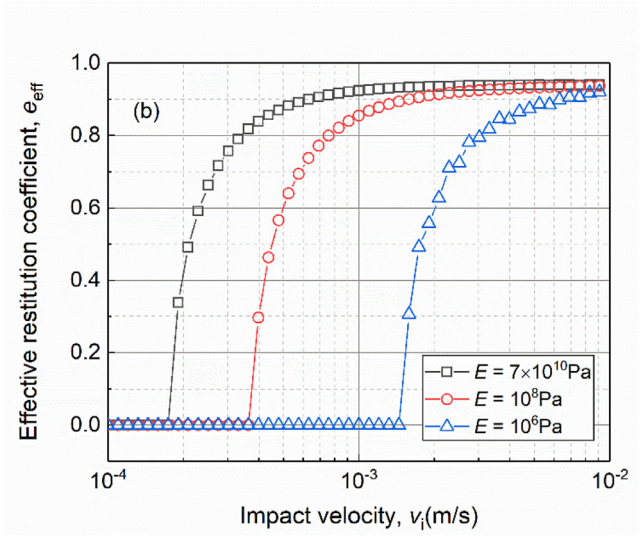

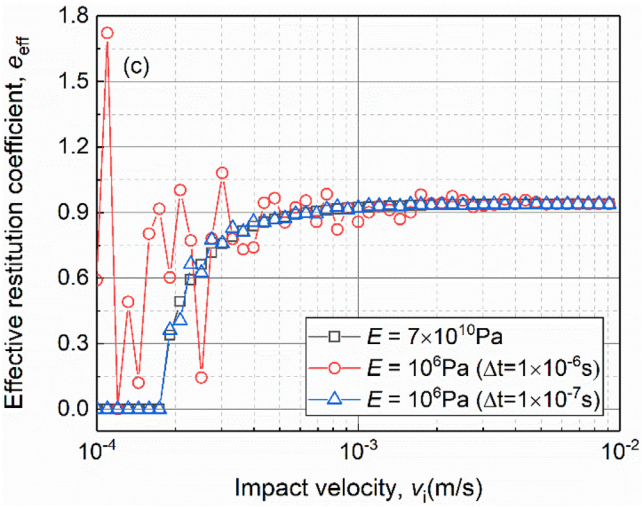

Fig. 3. Relationship between effective restitution coefficient and impact velocity, for (a) effect of non-contact van der Waals interaction, where the original particle Young's modulus ($Y = 7 \times 10^{10}$ Pa) is used, with a fixed timestep of 10^{-8} s, (b) effect of particle Young's modulus, where both contact and non-contact van der Waals interactions are considered and Hamaker constant is not scaled, (c) effect of DEM time step, where a reduced Hamaker constant is used for a reduced Young's modulus.

(see Fig. 1) and a poorly resolved non-contact van der Waals interaction. This is evidenced by a better agreement with the original particle stiffness, if further reducing the timestep to 10^{-7} s. However, it would cancel off the benefit of using a reduced particle stiffness. Therefore, it is necessary to propose an alternative approach for the calculation of non-contact van der Waals interaction.

The proposed prediction-correction scheme is also evaluated on head-on collisions between two particles. For two particles of same size and equal impact velocity, as shown in Fig. 4(a), the proposed scheme shows an excellent prediction of the original collision behaviour using reduced particle stiffnesses. Three different restitution coefficients of collision (e_n) are tested, all showing good agreement with the original particle stiffness. The test is further extended to collisions between particles of different sizes, with both equal (Fig. 4(b)) and non-equal (Fig. 4(c)) impact velocities. Stiffness independent results are obtained in all the tested cases, except only a slight discrepancy observed close to the critical impact velocity.

3.1.2. Particle moving on a flat surface

The modified calculations of sliding and rolling resistances (i.e. Eq. (41)) are evaluated by simulations of a sphere travelling on a flat surface. The simulation set-up is schematically shown in Fig. 5, where a sphere just touches the surface and is initialised with different translational velocities. For simplicity, particle rolling is first excluded (Fig. 5(a)) and then both sliding and rolling are enabled (Fig. 5(b)). In both cases, the sphere will stop after traveling for a certain distance due to the sliding and/or rolling resistances. The total distance travelled by the sphere is defined as the stop distance. The history of particle displacement is recorded. The original particle behaviour is compared with that using a reduced particle Young's modulus. The cases with and without the use of the modified normal contact force (i.e. Eq. (41)) in the calculations of sliding and rolling resistances are also compared. Here, normal restitution coefficient (e_n) is set to 0.6. Particle size is 60 μm. The original particle Young's modulus is 7×10^{10} Pa. Other parameters are the same as that of Table 1.

Fig. 6 shows the displacement history of a particle with an initial velocity of 0.001 m/s. As shown in Fig. 6(a) and Fig. 6(c), despite the use of a scaled contact adhesion (i.e. Eq. (38)), a reduced particle stiffness predicts a stop distance that is much larger than that of the original Young's modulus, confirming the inadequacy of the existing scaling approach to preserve original sliding and rolling behaviours. In contrast, the modified sliding and rolling resistances yield a prediction that follow roughly the same curve of the original particle stiffness in both cases, as shown in Fig. 6(b) and (d). The curve shows a nearly perfect quadratic slope, indicating a short damping period and hence an essentially constant deacceleration process.

Fig. 7 shows the predicted stop distances for three different initial velocities of 0.001 m/s, 0.01 m/s and 0.1 m/s. The modified sliding and rolling resistances are found to predict a stop distance that is very close to the original particle stiffness (7×10^{10} Pa), with the maximum difference less than 0.5% among all the tested velocities. It thus can be concluded that both the displacement evolution and the stop distance can be well captured by the present model.

3.2. Application to packing of fine particles

The developed scaling methodology is further applied to simulate the packing of fine particles. The simulation is carried out in a rectangular box with dimensions of $20d_p \times 20d_p \times 130d_p$, with d_p representing particle diameter. Periodic boundary conditions are applied in both in x and y directions. All particles are first generated randomly within the box with no overlap. An initial porosity of 90% is maintained to ensure consistency among different cases. Then, particles are deposited into the box under gravity. The packing process is terminated when kinetic energy of all particles has been dissipated. This packing method represents the so-called poured packing and has been widely used in the literature [41,42]. To assess the present scaling methodology, comparisons are made against the conventional DEM approach where force magnitude is evaluated based on the relative position between two interacting particles, which is typical in DEM modelling and has been widely used in simulations of fine particles [1,41–43].

3.2.1. Validation of the conventional DEM approach

For a valid comparison, it is necessary to ensure that results obtained by the current implementation of the conventional approach are valid and consistent with previous studies. This is done by comparing with literature results where the same force estimation method was used [1,41]. As an important macroscopic parameter, packing density is calculated after a stable packing is formed, according to,

$$\Phi = \frac{\sum \pi d_p^3/6}{L_x L_y (0.9 z_{\max} - z_{\min})} \tag{60}$$

where L_x and L_y are the dimension of the box in x and y direction, respectively. Only particles located within the range of $z_{\min}$ to $0.9z_{\max}$ are included in the summation, where $z_{\min}$ and $z_{\max}$ are the lower and upper limits of the packing in the gravitational direction.

Fig. 8 compares packing density obtained by the current implementation with the literature results [1]. Noting that contact adhesion and non-contact cohesive interaction is not distinguished in the previous work [1]. To calculate contact adhesion, instead of scaling the Hamaker constant adhesion, a relatively small value of Hamaker constant (6.5×10^{-20} J, corresponding to a surface energy of 0.862 mJ) was used, which can, to some extent, compensate the effect of the small

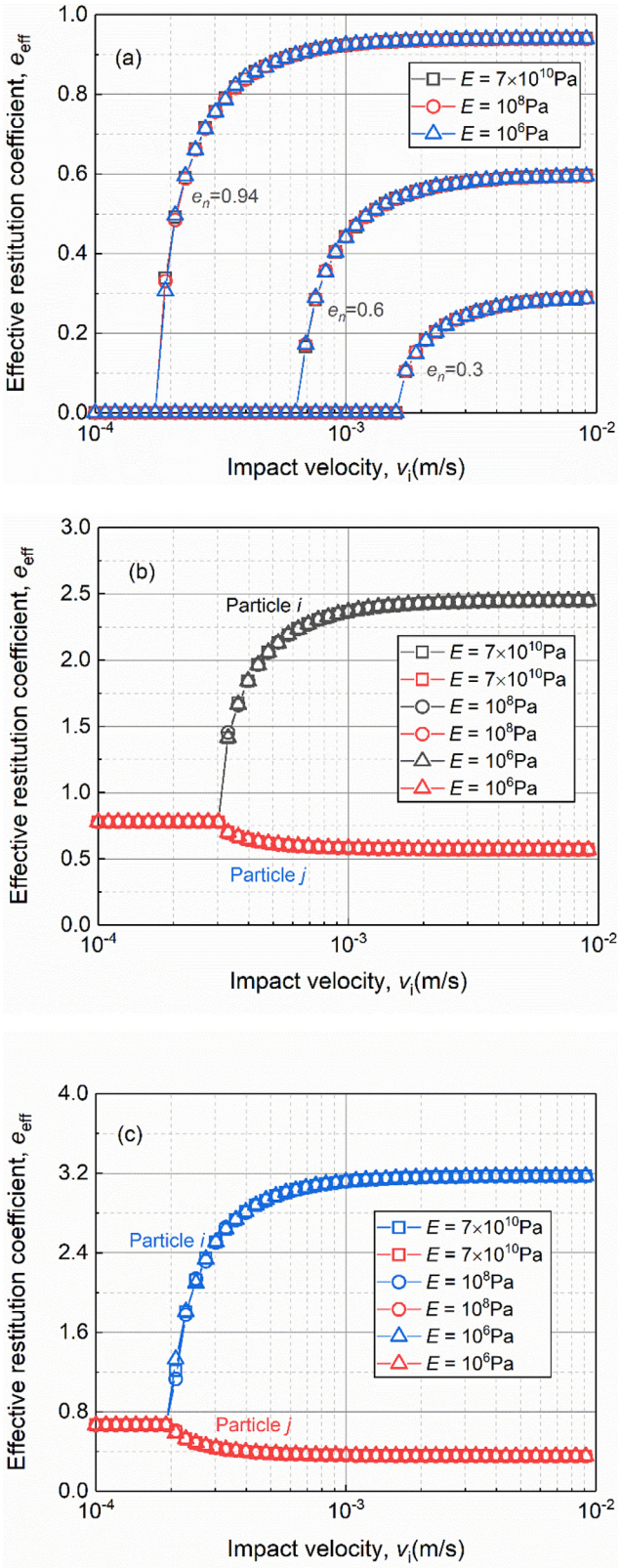

Fig. 4. Relationship between effective restitution coefficient and impact velocity when using the proposed impulse-based force estimation method for reduced Young's modulus, in which (a) head-on collisions between two particles with same size and impact velocity; and head-on collisions between two different sized particles (d_i = 30 μm and d_j = 60 μm), with (b) equal and (c) non-equal impact velocities (i.e. $|v_i| = 2|v_j|$).

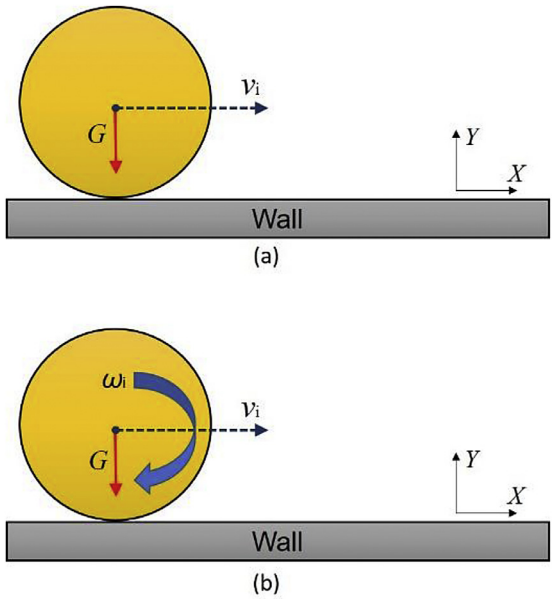

Fig. 5. Schematics of one particle (a) sliding and (b) sliding and rolling on a flat surface.

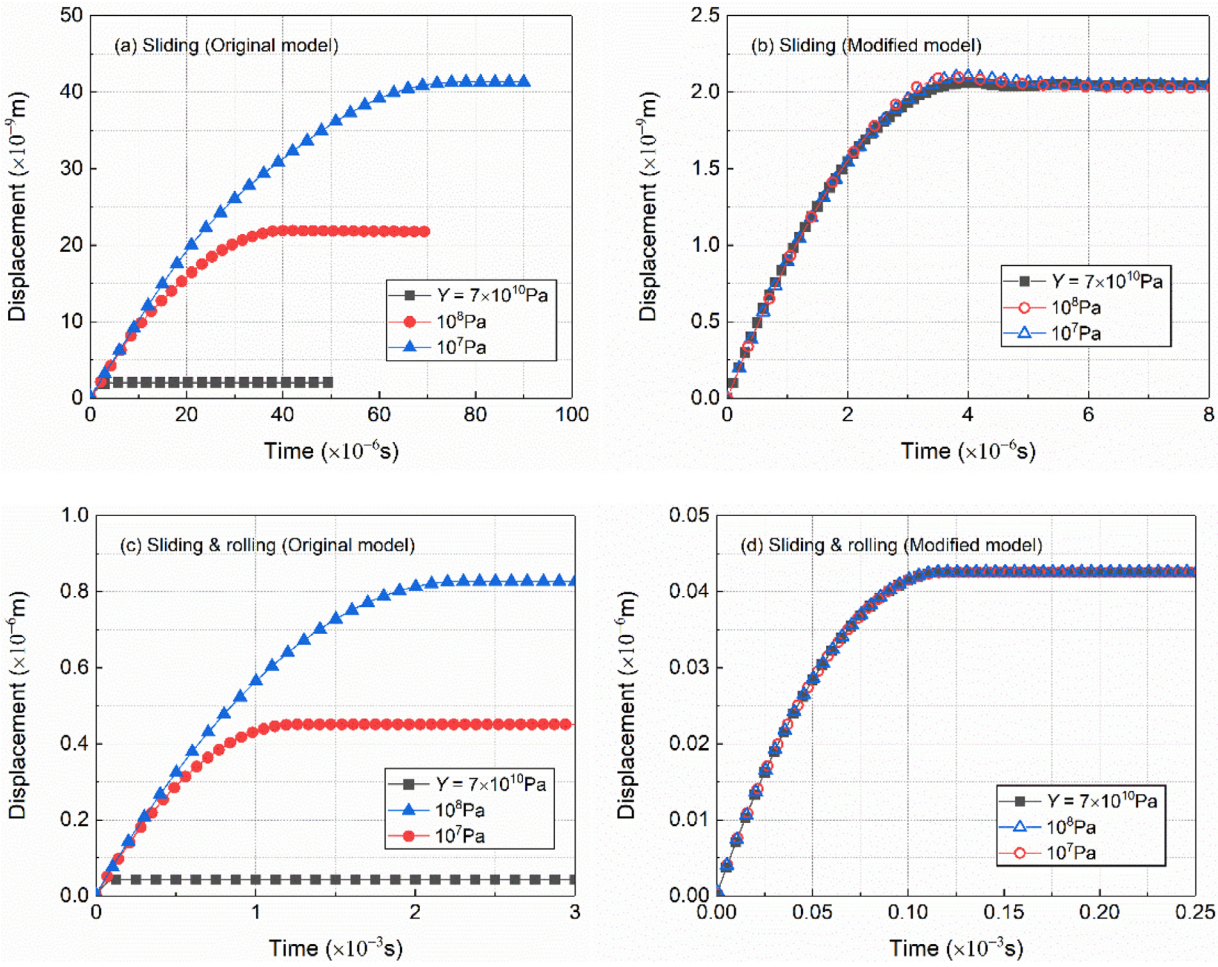

Fig. 6. Time history of particle displacement for an initial velocity of 0.001 m/s. Only sliding is enabled in (a) and (b) while both sliding and rolling are activated in (c) and (d).

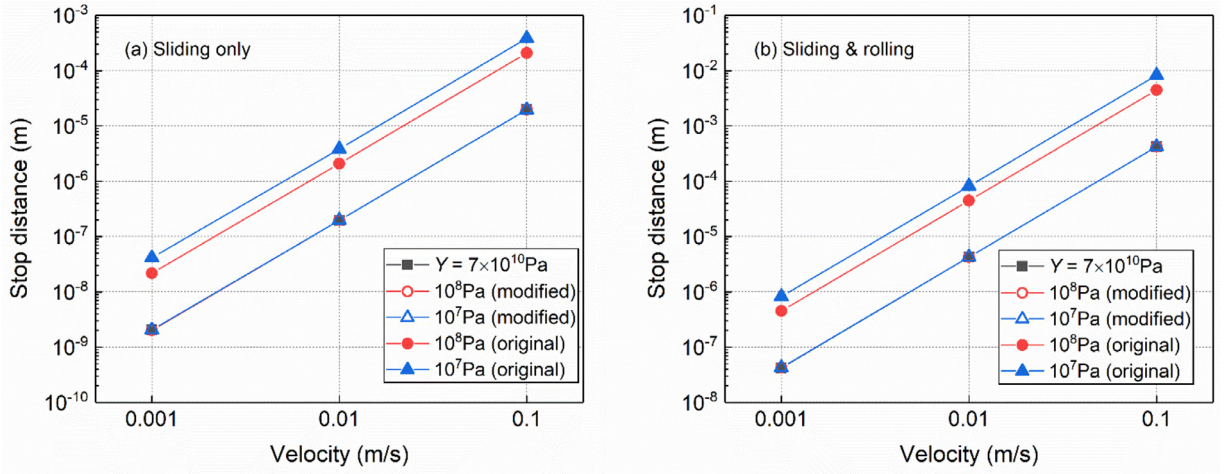

Fig. 7. Predicted stop distance of different initial translational velocities for (a) particles are only allowed to slide and (b) both sliding and rolling are enabled.

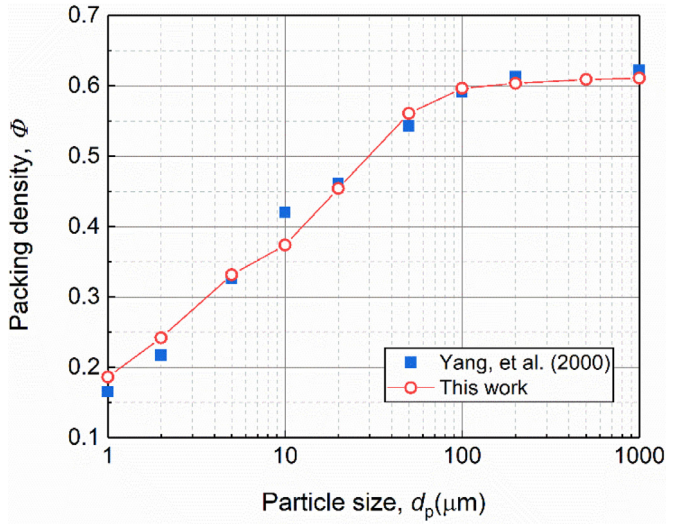

Fig. 8. Dependence of packing density on particle size: comparison between previous simulations [1] and the current implementation of the same model [1].

particle Young's modulus (i.e. 1.0 × 10^7 Pa) used in their study [1]. For validation purpose, the same modelling parameters [1] are used here. As shown in Fig. 8, packing density decreases monotonically with decreasing particle size when it is smaller than 100 μm, consistent with the previous results [1]. The same trend was also observed in experimental measurements [44] and modelling study using a JKR adhesion model [42]. The good agreement with the previous works confirms the validity of the current implementation of the conventional DEM approach, forming a valid basis for the evaluation of the present scaling methodology.

3.2.2. Performance evaluation

• **Simulation conditions**

Four groups of simulations are performed to evaluate the performance of the proposed method on packing. The modelling configurations are summarised in Table 3. Noting that, in all four groups, Hamaker constant (i.e. Eq. (38)) is scaled for contact adhesion while the original Hamaker constant is used for non-contact cohesion. In the first and second groups, only contact adhesion is considered (i.e. van der Waals interaction is only considered when two particles are in contact) while both contact adhesive and non-contact cohesion are considered in the third and fourth groups. Compared to the second and fourth groups, the modified sliding and rolling resistances (i.e. Eq. (41)) are introduced into the first and third groups of simulations. For the calculation of non-contact cohesion, the conventional force-estimation scheme is applied to the fourth group while the new prediction-correction scheme is applied to the third group of simulations.

Table 3
Model setup used in the simulation of particle packing.

Group	Model setup			
	Contact adhesion	Non-contact cohesive interaction	Modified sliding and rolling (Eq. (24))	New force estimation scheme (Eq. (41))
1	Yes	/	Yes	/
2	Yes	/	/	/
3	Yes	Yes	Yes	Yes
4	Yes	Yes	/	/

Table 4
Parameters used in the simulation of particle packing.

Parameter	Values
Particle number, N_p	10,000
Particle density, ρ_p (kg/m^3)	2500
Young's modulus, Y(Pa)	6.3×10^{10}
Poisson's ratio, ν	0.24
Sliding friction coefficient, μ_s	0.5
Rolling friction coefficient, μ_r	0.002
Restitution coefficient, e	0.6
Hamaker constant, A(J)	1.0×10^{-19}
Minimum cut-off distance, $s_{\min}$ (m)	1.65×10^{-10}

Table 5
Particle size tested and its corresponding Bond number (Bo_g).

Particle diameter (μm)	80	40	20
Particle Bond number, Bo_g	1.86×10^3	7.45×10^3	2.98×10^4

The simulation parameters listed in Table 4 are the same as those used in the study of Parteli et al. [35] for silica glass particles. Different from the previous work [35], rolling resistance is included here to account for the effect of asymmetrical distribution of contact pressure, as typically considered in many packing studies. Therefore, quantitative agreement with the previous work is not aimed here. Instead, focus is given to the effect of stiffness scaling on the packing structure. Three different particle sizes are tested here. The cohesive strength is quantified by a modified Bond number defined as the ratio of the maximum adhesive force to particle gravity (i.e. $Bo_g = |\mathbf{F}_v^{\max}|/mg$). The tested particle sizes and their corresponding Bond numbers are given in Table 5.

• **Packing density**

As an illustration, Fig. 9 shows the finial packing simulated by the proposed models (*group 3*) of three particle diameters: 20 μm, 40 μm and 80 μm. It can be seen from the height of the packing that smaller particle size results in a much loose packing structure than the larger ones, which is in line with the previous observation [1].

Fig. 10 shows the packing density as a function of stiffness scaling ratio. Clearly, a large particle size results in a higher packing density. The same trend is observed among all groups of simulations. Despite using a scaled Hamaker constant in the calculation of contact adhesion, the second and fourth groups predicted an increase of packing density with decreasing scaling ratio, irrespective of particle sizes. The predicted packing density can be 1.4 times larger than that of the original properties with a particle size of 40 μm and a scaling ratio of 0.001. The previous scaling approach (i.e. only applying the scaling law of Eq. (38)) is thus not able to capture the original packing density. This is further confirmed by the first group of simulations where the modified normal contact force (i.e. Eq. (41)) is introduced to calculate sliding and rolling resistances. For all the tested cases, the maximum difference relative to the original packing density is 4.25% for the size of 80 μm, 5.06% for 40 μm and 3.96% for 20 μm. A stiffness-insensitive packing density can be obtained down to a scaling ratio of 0.001, further highlighting the critical importance of correcting the sliding and rolling resistances in stiffness scaling.

The third and fourth groups consider both contact adhesion and non-contact cohesion, with a difference in handling the calculation of non-contact cohesion. Comparing the second and fourth groups, density difference induced by the non-contact cohesion is found to be dependent on both scaling ratio and particle size. A large variation with scaling ratio can be observed for the size of 80 μm while a more stable difference is observed for 20 μm, which may be caused by the difference in DEM timestep. In contrast, the density difference becomes less sensitive to the scaling ratio in the third group of simulations where the new prediction-correction scheme was used. Compared to the original packing density (i.e. without scaling), the new scheme gives a relative difference smaller than 0.35% for the size of 80 μm, 0.38% for 40 μm and 0.04% for 20 μm, confirming its validity in calculating the non-contact van der Waals interaction.

• **Coordination number**

A more detailed understanding of the impact of the proposed approach on packing structure can be obtained by looking at the particle coordination number (*CN*) defined as the number of particles in contact with a given particle. Fig. 11 shows

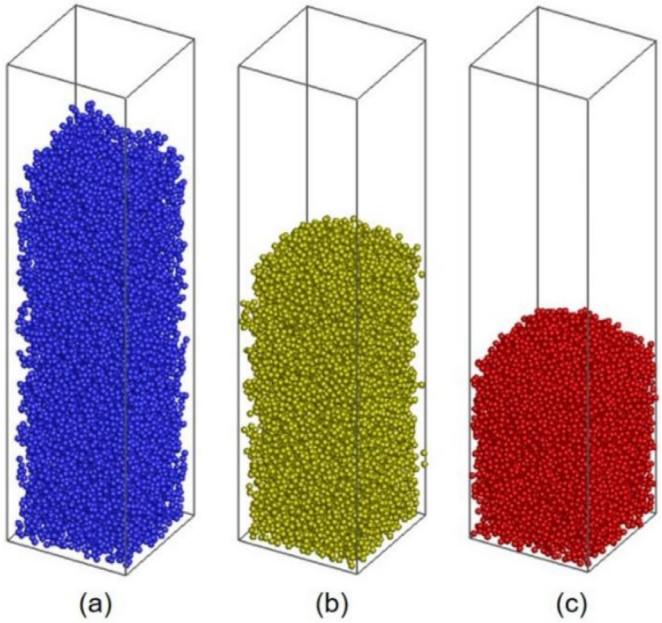

Fig. 9. Numerical simulation of the packing of spherical particles. Figs. a–c show snapshots of the packing of spherical particles with diameter of (a) 20 μm, (b) 40 μm and (c) 80 μm.

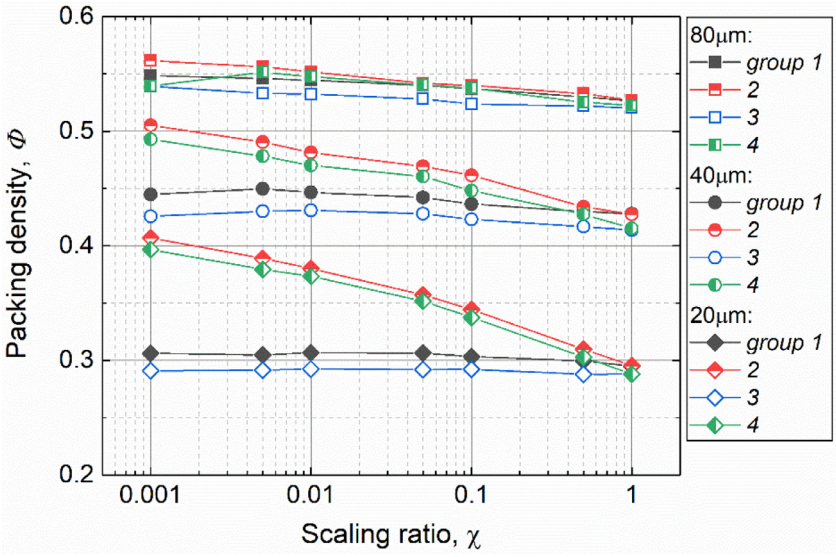

Fig. 10. Packing density as a function of scaling ratio of particle stiffness.

the dependence of the average coordination number on the scaling ratio of particle stiffness. It should be noted that coordination number is sensitive to the critical distance of separation chosen to define whether two particles are in contact. The critical distance of separation is set to $1.005d_p$ in the work of Yang et al. [1], which is also adopted here. It can be seen from Fig. 11 that the mean coordination number decreases with decreasing particle size. The same trend is preserved in all groups of simulations. With decreasing particle size, the van der Waals force becomes the dominant force, counteracting the gravity force for densification. The densification due to sliding and rolling is also largely prohibited for small particles. For the particle size of 20 μm, the mean coordination number is around 2.8, indicating the formation of chain-like structure which can also be observed from Fig. 9(a). Clearly, there is a positive correlation between packing density and average coordination number within each group of simulations. Comparing the results across different simulation groups, the present model demonstrates superior performance in predicting packing structure using a reduced particle stiffness. As shown in the first and third groups, the average coordination number remains largely the same across all the tested scaling ratios, indicating

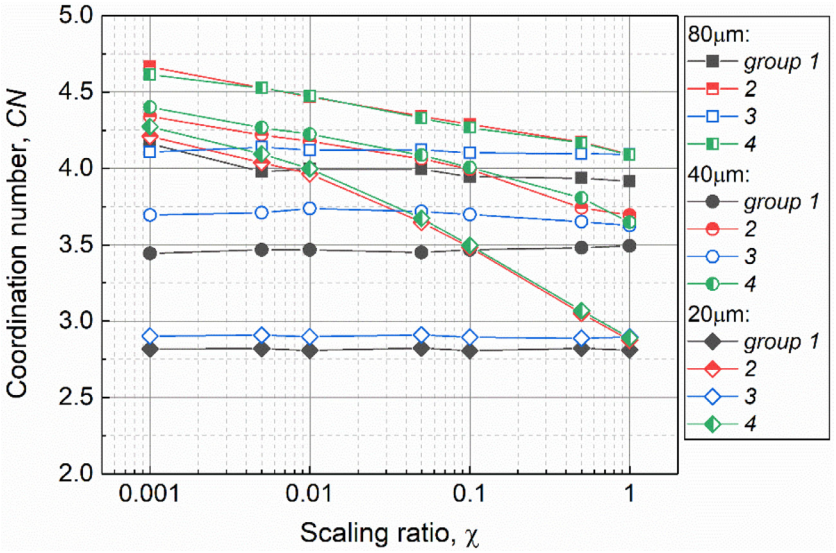

Fig. 11. The dependence of mean coordination number on the ratio of reduced particle Young's modulus.

that corrections to the sliding and rolling resistances are essential to achieve a successful scaling. It is also interesting to find that introducing non-contact cohesive interaction slightly increases the average number of contacts, confirming that it is essential to consider this short-ranged non-contact attractive force for the prediction of packing structure.

• **Packing structure**

The resulting packing structure can be further analysed statistically by the distributions of coordination number and local packing density. The local packing density is calculated as the ratio of the particle volume to the volume of the Voronoi cell associated with it. Voronoi analysis is an effective tool to understand pore network and has been used to study transport properties of a packing [41]. Fig. 12 shows the frequency distribution of coordination number and local packing density of the packing of 40 μm particles using the proposed DEM approach. The coordination number varies from 1 to 7, with its mode equal to 4. The difference between different scaling ratios are very small for both coordination number and local packing density. The results are also close to that of the original particle properties calculated using the conventional DEM method, further confirming the validity of the proposed model in predicting packing structure of fine particles using reduced particle stiffness.

3.3. Model applicability

The applicability of the proposed approach is evaluated by performing a series of simple shear simulations over a range of controlled pressures, with a focus on the prediction of steady-state volume fraction and stress ratio. The simulation configuration is illustrated in Fig. 13, with Lees-Edwards periodic boundary applied [45] in the z direction and normal periodic conditions in the x and y directions. For simplicity, mono-size spherical particles of 100 μm are used and all the simulations are performed in the absence of gravity. Assemblies of 8000 particles are sheared under a specified shear rate of $\dot{\gamma}$, giving a velocity of $U\ (=\dot{\gamma}L/2)$ at the top and the bottom boundaries. Throughout the simulation, the macroscopic stresses are calculated as a summation of the contributions from both velocity fluctuation and interparticle forces [46].

$$\sigma = \frac{1}{V}\sum_{i}\left[\sum_{j\neq i} l_{ij}\mathbf{F}_{ij} + m_i\left(\mathbf{v}_i^{'}\right)\left(\mathbf{v}_i^{'}\right)\right] \tag{61}$$

with V the box volume, l_{ij} the branch vector pointing from the contact point between particle j and particle i to the centre of particle i. $\mathbf{F}_{ij}$ is the force acting on particle i due to particle j. $\mathbf{v}_i'$ is the fluctuating velocity of the particle. The stress ratio is defined as a ratio of ensemble-averaged shear stress (σ_{xz}) to pressure ($(\sigma_{xx}+\sigma_{yy}+\sigma_{zz})/3$).

Due to the presence of cohesive interaction, it is difficult to maintain a homogeneous shearing at low volume fractions (for example, $\Phi < 0.55$) [40]. Therefore, the approach proposed in the study of Shi et al. [15] is adopted to ensure a homogeneous shearing by moving all the particles at each timestep. The validation of the implementation of Lees-Edwards periodic boundaries can be found in Appendix A.3. To achieve a pressure-controlled shearing, the normal stress P (i.e. σ_{zz}) is kept constant by allowing the box to either dilate or contract along the z direction. Particle properties are the same as that in Table 4, except varying the Hamaker constant to give different levels of interparticle cohesion.

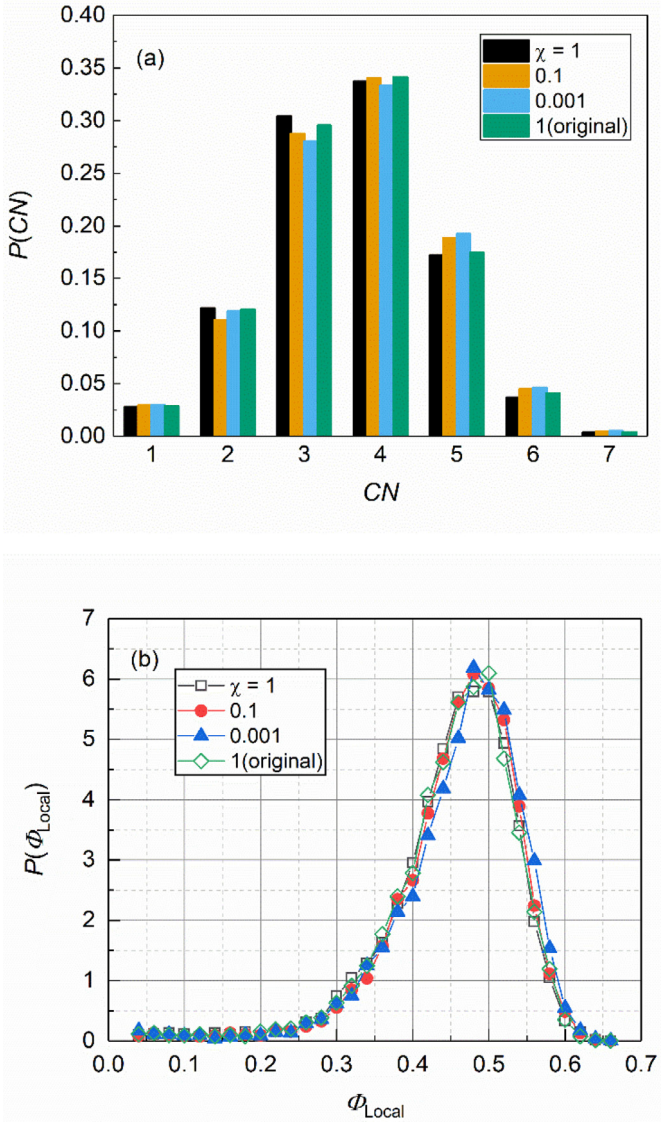

Fig. 12. Distributions of (a) coordination number and (b) local packing density for different reduced ratios of particle Young's modulus of the packing of 40 μm spherical particles.

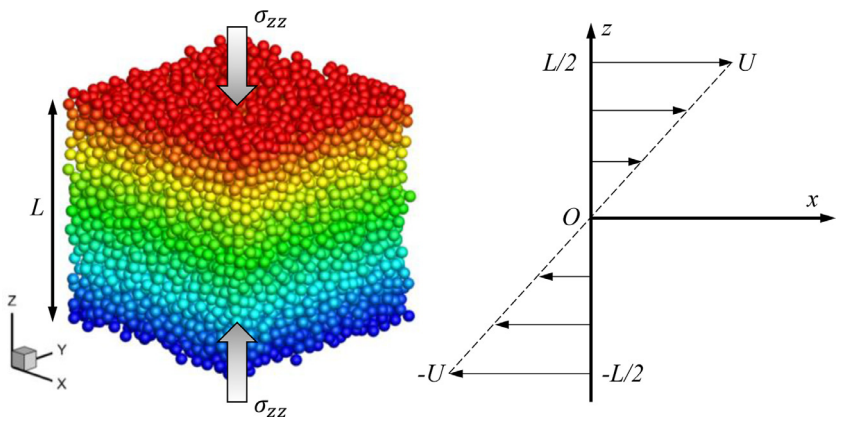

Fig. 13. Simulation configuration of simple shear box. *L* is the dimension of the domain in the *z* direction and particles are coloured by the velocity in the x direction. (For interpretation of the references to colour in this figure, the reader is referred to the web version of this article.)

Table 6
Control parameter used in the simulation of simple shear box.

Parameter	Values
Hamaker constant, A (J)	2.1×10^{-21}, 2.1×10^{-20}, 2.1×10^{-19}
Stress, P (Pa)	50 – 10^5
Shear rate, $\dot{\gamma}$ (s^{-1})	1, 10, 100
Contact Bond number, Bo_c	10^{-9}, 10^{-8}, 10^{-7}
Particle Bond number, Bo_g	26, 260, 2600
Dimensionless control pressure, P^*	1.5×10^{-9} – 3.0×10^{-6}
Dimensionless shear rate, $\widehat{\dot{\gamma}}$	2.73×10^{-8}, 2.73×10^{-7}, 2.73×10^{-6}

Control parameters are varied to examine the model applicability, including pressure, shear rate and particle cohesion. For each case, particle stiffness is scaled down to four orders of magnitude. For a simple shear simulation, two global time scales can be defined,

$$t_{\dot{\gamma}} = 1/\dot{\gamma} \tag{62}$$

$$t_p = d\sqrt{\rho/P} \tag{63}$$

which are related to the shear rate and pressure, respectively. The control pressure can be made dimensionless by scaling with a characteristic contact pressure (i.e. $P^* = P/E^*$) and a dimensionless shear rate is defined as $\widehat{\dot{\gamma}} = \dot{\gamma}d/\sqrt{E^*/\rho}$, same as that used in previous studies [15]. The dimensionless pressure can be viewed as the square of the ratio between a time scale related to contact stiffness (i.e. $t_k = \sqrt{\rho d^2/E^*}$) and pressure timescale t_p (i.e. $P^* = (t_k/t_p)^2$) while the dimensionless shear rate can be viewed as ratio of t_k to $t_{\dot{\gamma}}$ (i.e., $\widehat{\dot{\gamma}} = t_k/t_{\dot{\gamma}}$). Due to the absence of gravity, a modified contact Bond number, Bo_c, is used here to quantify the cohesive strength (i.e. $Bo_c = |\mathbf{F}_v^{\max}|/(E^*d^2)$) [40]. Table 6 lists the input range of the control parameters. The Bond number based on particle gravity (Bo_g) is also given, despite not relevant here.

3.3.1. Effect of cohesive strength

Fig. 14 plots the steady-state volume fraction and stress ratio against the scaled shear rate for samples with different contact Bond numbers (Bo_c). Noting that these results are predicted by the original particle properties. The steady-state volume fraction increases with control pressure while the stress ratio decreases with it, with both approaching asymptotic values at large pressures. For a given control pressure, the volume fraction always decreases with the contact Bond number (Bo_c). This is because particle cohesion can enhance the role of friction due to an enhanced local compressive stress, thus leading to strong dilatancy of the sample under shearing. Increasing control pressure, however, suppresses the role of particle cohesion, as the local compressive stresses acting at the particle contacts are increasingly contributed by the external pressure. Particle cohesion increases the stress ratio. With a large Bond number (i.e. 10^{-7}), the stress ratio can be larger than 1.0 at small control pressures, which is also reported in the previous studies [14,47].

Fig. 15 shows the performance of the proposed approach in predicting steady-state volume fraction and stress ratio for samples of different contact Bond numbers (Bo_c). The colour-coded number represents the maximum order of magnitude κ ($= \log\chi$) to which the particle stiffness can be safely reduced, where a difference smaller than 5% relative to that of the original particle stiffness can be obtained. The performance is found to deteriorate at a very large scaled pressure (i.e. ≥3.0e-7). It can be attributed to the fact that particles with a reduced stiffness allows large overlaps to be formed between particles under high pressures. A strong cohesion also leads to a reduced performance, especially for the prediction of stress ratio. For the largest contact Bond number tested here (i.e. Bo_c=1.0e-7), the proposed scaling methodology performs poorly at a moderate scaled pressure (i.e. 1.5e-8) for the prediction of steady-state volume fraction and fails to predict the stress ratio when the scaled pressure is smaller than 3.0e-8.

From the above analysis, one can see that the performance of the proposed approach is controlled by both particle cohesion and external pressure. In the following, we try to link the model performance with the maximum allowable overlap between particles. For a given external pressure P, the typical contact force is of order Pd^2, with d particle diameter. The relative importance between particle cohesion and external pressure can be quantified by a system Bond number defined as,

$$Bo_s = |\mathbf{F}_v^{\max}|/\left(Pd^2\right) \tag{64}$$

which basically measures system cohesiveness [15]. According to the Hertzian contact law (i.e. Eq. (5)) and considering the presence of cohesive interaction,

$$(1 + Bo_s)Pd^2 \sim E^*\sqrt{d}\delta^{3/2} \tag{65}$$

A dimensionless overlap can then be determined as,

$$\delta^* = \frac{\delta}{d} = \left(\frac{(1 + Bo_s)P}{E^*}\right)^{2/3} \tag{66}$$

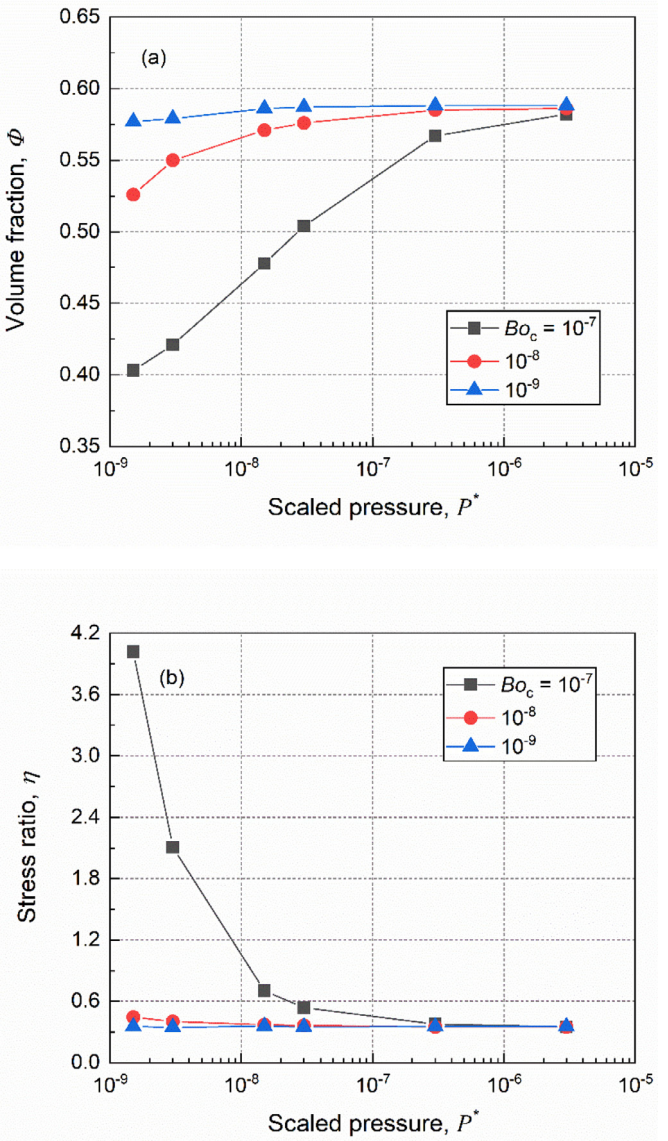

Fig. 14. Steady-state (a) volume fraction and (b) steady-state stress ratio as a function of scaled control pressure for different Bond numbers, with a dimensionless shear rate of 2.73×10^{-7}.

(a) Volume fraction		Bond number		
		1.0E-09	1.0E-08	1.0E-07
Scaled pressure	1.5E-09	4	4	2
	3.0E-09	4	4	2
	1.5E-08	4	4	1
	3.0E-08	4	4	2
	3.0E-07	3	3	3
	3.0E-06	2	2	2

(b) Stress ratio		Bond number		
		1.0E-09	1.0E-08	1.0E-07
Scaled pressure	1.5E-09	4	0	0
	3.0E-09	3	2	0
	1.5E-08	4	4	0
	3.0E-08	4	4	0
	3.0E-07	3	4	3
	3.0E-06	2	2	3

Fig. 15. Model performance for the prediction of (a) volume fraction and (b) stress ratio using reduced particle stiffness. (For interpretation of the references to colour in this figure, the reader is referred to the web version of this article.)

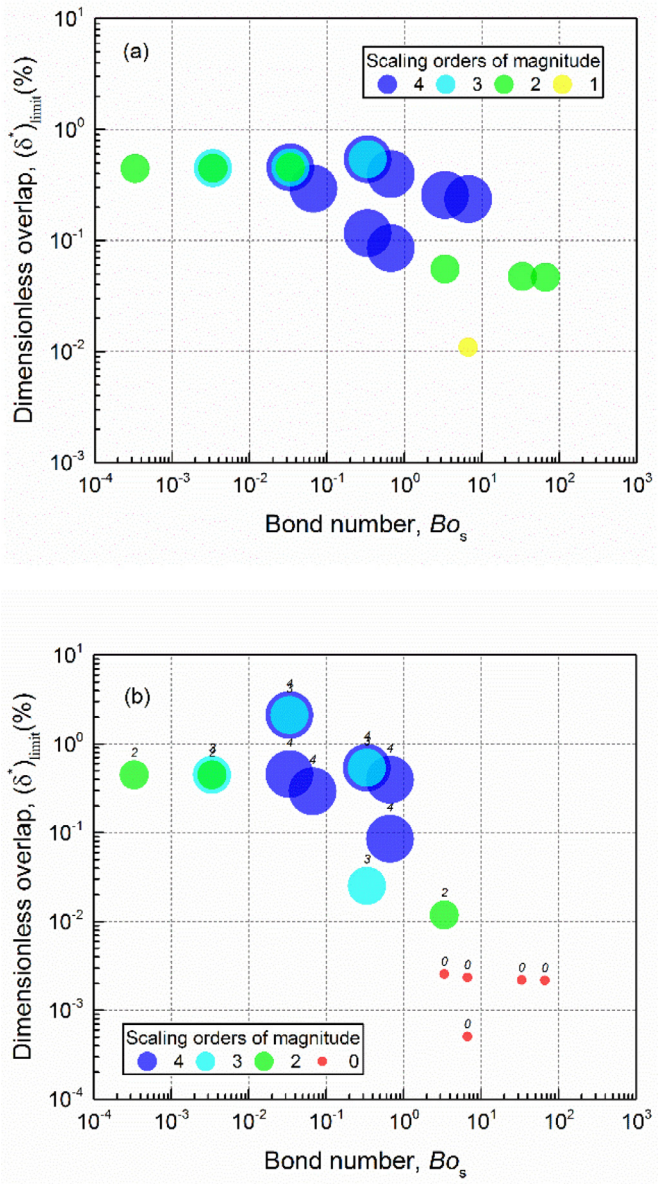

Fig. 16. Relationship between the limiting dimensionless overlap and the modified Bond number (Bo_s) in the prediction of (a) volume fraction and (b) stress ratio.

If we assume particle stiffness can be safely reduced χ times, the limiting dimensionless overlap after stiffness scaling can then be estimated as,

$$(\delta^*)_{\text{limit}} = ((1 + Bo_s)P^*\chi)^{2/3} \tag{67}$$

where $P^* = P/E^*$ and E^* is calculated based on the original particle stiffness.

Based on the results in Fig. 15, the dependence of the limiting dimensionless overlap ($(\delta^*)_{\text{limit}}$) on the modified Bond number (Bo_s) is plotted in Fig. 16. The prediction of stress ratio is clearly more sensitive to the system cohesiveness than that of the volume fraction. For a weakly cohesive system (i.e. $Bo_s<0.1$), the maximum allowable scaling ratio can be determined by setting a limiting dimensionless overlap to 0.5% for the predictions of both volume fraction and stress ratio. For a moderately cohesive system (i.e. $0.1<Bo_s<10$) where pressure level and particle cohesiveness are comparable, stiffness scaling should be applied with cautious, especially for the prediction of stress responses. This is mainly caused by the steady-state approximation adopted in the modified sliding and rotating resistances. For a strongly cohesive system (i.e. $Bo_s>10$), a limiting dimensionless overlap of 0.05% can be suggested for the prediction of steady-state volume fraction. One can see from Eq. (66) that, for a given limiting dimensionless overlap, the maximum allowable scaling ratio is inversely

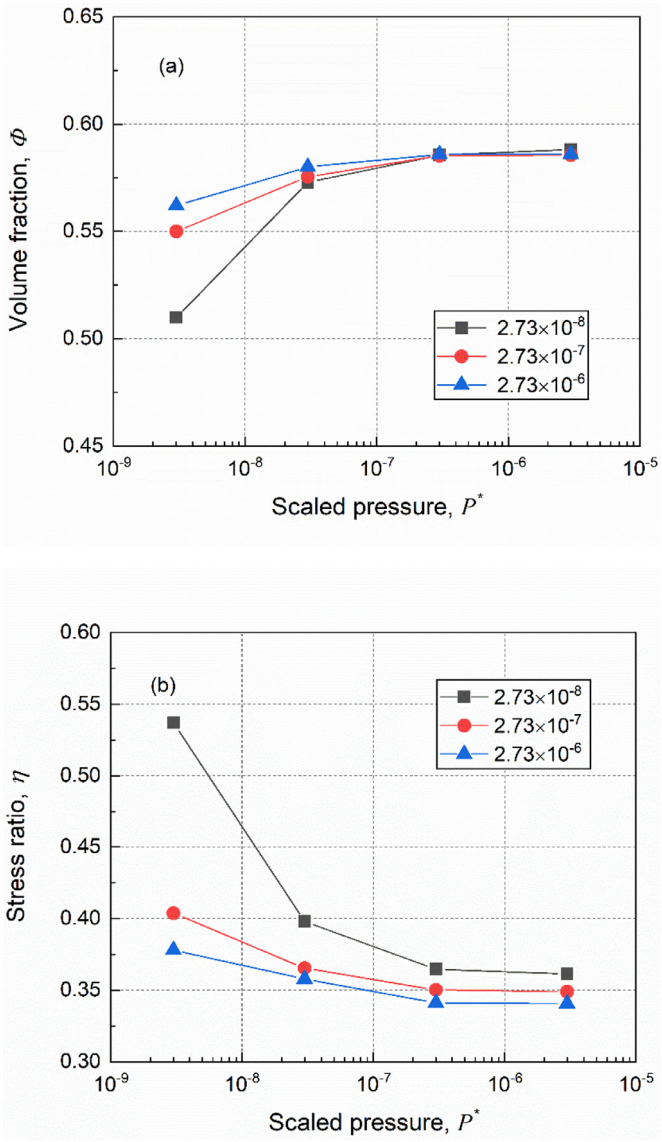

Fig. 17. Steady-state (a) volume fraction and (b) steady-state stress ratio as a function of scaled control pressure under different dimensionless shear rates, with a contact Bond number (Bo_c) of 10^{-8}.

related to system cohesiveness and pressure level, which is probably why the particle stiffness can be safely reduced four orders of magnitude for packing (as shown in Section 3.2), as pressure in packing is contributed by particle gravity.

3.3.2. Effect of shear rate

Fig. 17 shows the effect of shear rate on the steady-state volume fraction and stress ratio as a function of the dimensionless pressure. Here, the contact Bond number (Bo_c) is fixed to 10^{-8}. Increasing shear rate is found to increase the volume fraction but decreases the stress rate. For a given pressure, increasing shear rate leads to an enhanced particle mobility, hence leading to a denser packing before reaching the jamming point.

Fig. 18 shows the effect of shear rate on the model performance, in which the shaded number denotes the maximum allowable orders of stiffness reduction. The model performance is correlated positively to the shear rate, especially for the prediction of stress ratio. In contrast, the prediction of volume fraction mainly depends on the pressure level, with reduced performance observed under large pressures.

The dependence of the model performance on shear rate can be related to the dominant contact mode. The dimensionless shear rate is related to the shearing timescale $t_{\dot{\gamma}}$, which measure the time required for particle rearrangement under a certain shear rate. A decrease in the dimensionless shear rate results in an increase in $t_{\dot{\gamma}}$, which indicates a shift of the contact mode from collision-dominant to enduring-contact. In contact-dominant systems, frictional interaction becomes crit-

(a) Volume fraction		Shear rate		
		2.73E-08	2.73E-07	2.73E-06
Scaled pressure	3.0E-09	2	4	4
	3.0E-08	4	4	4
	3.0E-07	3	3	3
	3.0E-06	2	2	2

(b) Stress ratio		Shear rate		
		2.73E-08	2.73E-07	2.73E-06
Scaled pressure	3.0E-09	2	2	4
	3.0E-08	2	4	4
	3.0E-07	3	4	4
	3.0E-06	2	2	3

Fig. 18. Model performance for the prediction of (a) volume fraction and (b) stress ratio under different shear rates and control pressures.

ical. The steady-state assumption introduced in the modified sliding and rolling resistances thus come into play and causing a reduced model performance. It is interesting to note that, for a given shear rate, the model performance deteriorates at low pressures. This is mainly caused by the system Bond number (i.e. Bo_s) which increases from 3.34e-3 to 3.34 when the dimensionless pressure decreases from 3.0e-6 to 3.0e-9. As discussed before, the contact pressure and the adhesive force are comparable when $1.0<Bo_s<10$, which leads to a reduced model performance. However, a large pressure also leads to reduced performance if interparticle overlap becomes too large (i.e. P^*=3.0e-6).

4. Conclusion and outlook

Application of DEM modelling to cohesive fine particles is often limited by a high computational cost, which promotes the use of a reduced particle stiffness to speed up calculations. However, the previously proposed stiffness scaling approaches were found to have several issues, especially for contact-dominated systems, leading to under-predicted sliding and rolling resistances and a poorly resolved non-contact van der Waals interaction. This paper thus proposed a new methodology to overcome these issues based on analysis of the dimensionless governing equations of motion. It consists of three key components: an established scaling law for contact adhesion (i.e. Eq. (38)), a modified calculation of sliding and rolling resistances using an adjusted normal contact force based on steady-state approximation (i.e. Eq. (41)), and a new prediction-correction scheme for the calculation of non-contact van der Waals interaction (i.e. Eq. (59)), which allows an enlarged timestep to be used with reduced particle stiffness. The main findings are summarised as follows,

- The new approach was examined by a series of simple verification tests, including head-on collision between two particles, oblique particle–wall collision, and particle-agglomerate collisions, with all showing stiffness-independent collision outcomes, which confirms capability of the proposed prediction-correction scheme in handling non-contact van der Waals interaction.
- With the modified sliding and rolling resistances, the predicted stop distance of a particle sliding and/or rolling over a flat surface was preserved when the stiffness was scaled down almost four orders of magnitude, which was not possible with the existing scaling approaches.
- The validity of proposed scaling methodology was evaluated on the packing of fine particles. The proposed approach outperforms the conventional DEM method, showing stiffness-independent results on both global packing density and detailed packing structure.
- Applicability of this approach was explored by simulations of homogeneous stress-controlled simple shearing under a series of pressures, particle cohesions and shear rates. The model performance can be related to a typical dimensionless overlap within the sample of a reduced particle stiffness. Empirical correlation and critical values have been proposed to determine the maximum allowable stiffness scaling ratio. However, it should be applied with cautious for the case where pressure level and particle cohesion are comparable.

Although only van der Waals interaction is discussed here, the proposed approach can also be extended to other types of cohesive interactions, especially for the presence of non-contact interaction. The present model shows strong potential to accelerate simulations of cohesive fine particles. However, it is worthwhile to further explore its applicability and to test its validity in other particulate systems. This approach is currently being applied to powder spreading and will be reported soon.

Declaration of Competing Interest

The authors declare that they have no known competing financial interests or personal relationships that could have appeared to influence the work reported in this paper.

CRediT authorship contribution statement

Yi He: Conceptualization, Methodology, Software, Investigation, Validation, Formal analysis, Visualization, Writing - original draft, Writing - review & editing. **Ali Hassanpour:** Writing - review & editing. **Mohammadreza Alizadeh Behjani:** Writing - review & editing. **Andrew E. Bayly:** Writing - review & editing, Investigation, Supervision, Funding acquisition.

Acknowledgements

The authors would like to acknowledge the financial support from the EPSRC-UK MAPP Future Manufacturing Hub (EP/P006566/1, www.mapp.ac.uk). This work was undertaken on ARC3, part of the high-performance computing facilities at the University of Leeds, UK. The first author would like to thank Dr. Yang Cui from the University of Edinburgh and Dr. Hao Shi from the University of Twente for their helpful discussion on the implementation of Lees-Edwards boundary condition.

Appendix

A.1. Oblique collision between particle and wall

Oblique particle–wall collision is also simulated to test the proposed force-estimation scheme, as schematically shown in Fig. 19. The initial distance between particle and wall is set to 1.2 times of its radius. The normal restitution coefficient of collision (e_n) is also varied. In these examples, particle rolling is excluded for simplicity. The effective restitution coefficient for an original particle Young's modulus of 7.0×10^{10} Pa is compared with that scaled down by serval orders of magnitude to 10^6 Pa.

As shown in Fig. 20, the effective restitution coefficient follows a same curve for both the original and the reduced particle stiffness, irrespective of the impact angle. The quantitative agreements are satisfactory, indicating the present model is also able to handle the calculation of non-contact van der Waals interaction between particle and wall.

A.2. Collisions between one particle and a string of particle

To test the performance of dealing with agglomerates, a set-up the same as that used in the study of Gu et al. [30] is adopted here. As shown in Fig. 21, one particle collides with a string of 15 stationary particles at an initial velocity of 0.02 m/s. Particles are positioned next to each other. The steady velocity after collision are sampled. To compare with Gu's model, the performance of a linear Hookean contact model is also presented. For the Hookean contact model, the original particle stiffness is 7000 N/m. For the Hertzian contact model, the original particle Young's modulus is 7×10^{10} Pa.

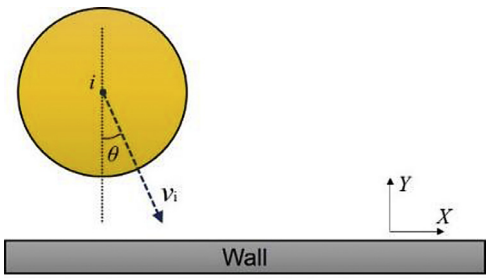

Fig. 19. The schematic of one particle impact with a stationary wall, where the particle is located $1.2R_i$ away from the wall.

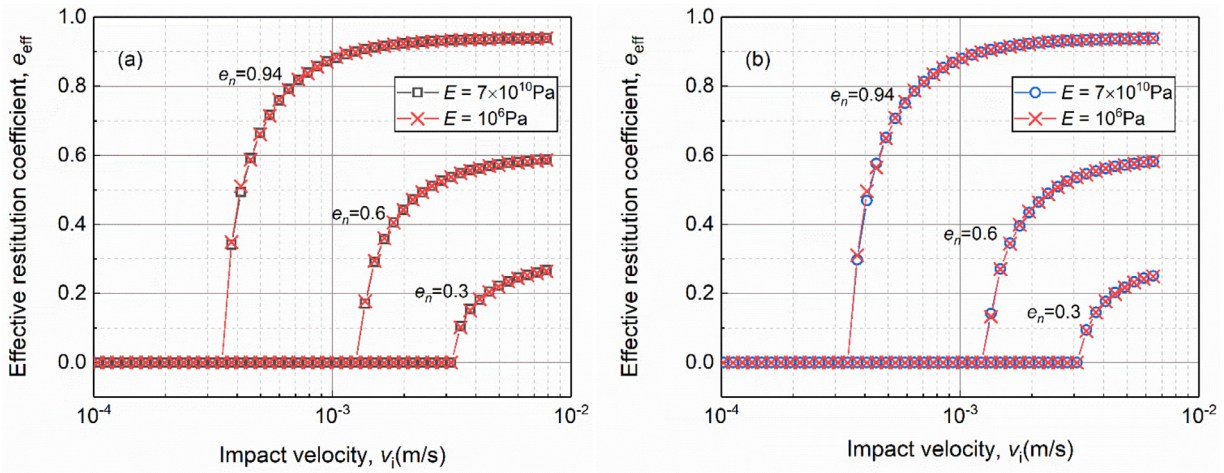

Fig. 20. Relationship between effective restitution coefficient and impact velocity for E=7.0 × 10^{10} Pa and E=1.0 × 10^6 Pa. The size of particles is 60 μm. The impact angle is set as (a) 30 degree and (b) 45 degree.

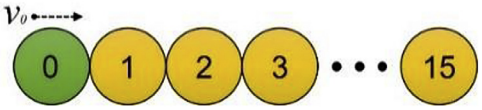

Fig. 21. Schematic of one particle impact with a string of 15 particles.

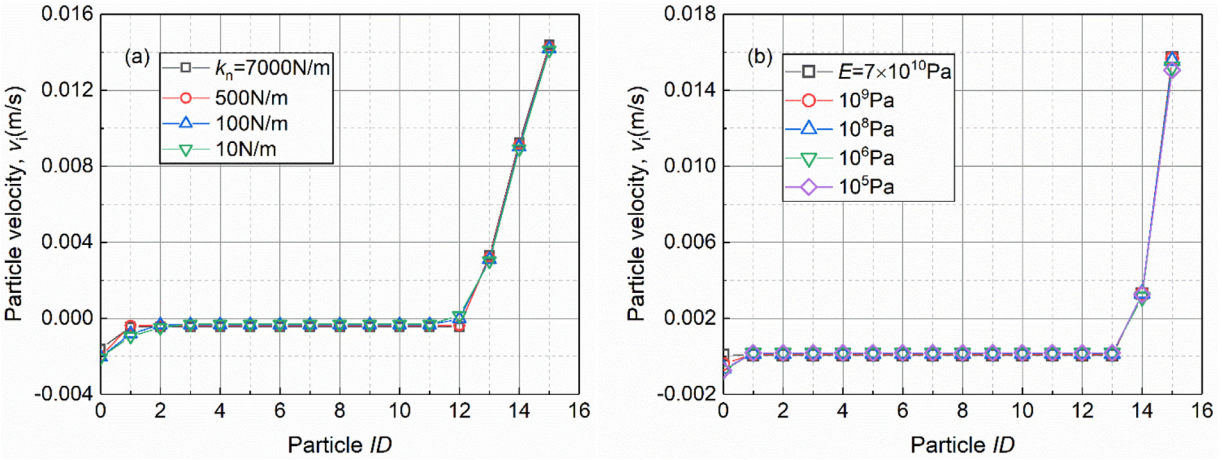

Fig. 22. Distribution of post-collision particle velocities in the collision between one particle and a string of particles, with (a) the Hookean contact model and (b) the Hertzian contact model.

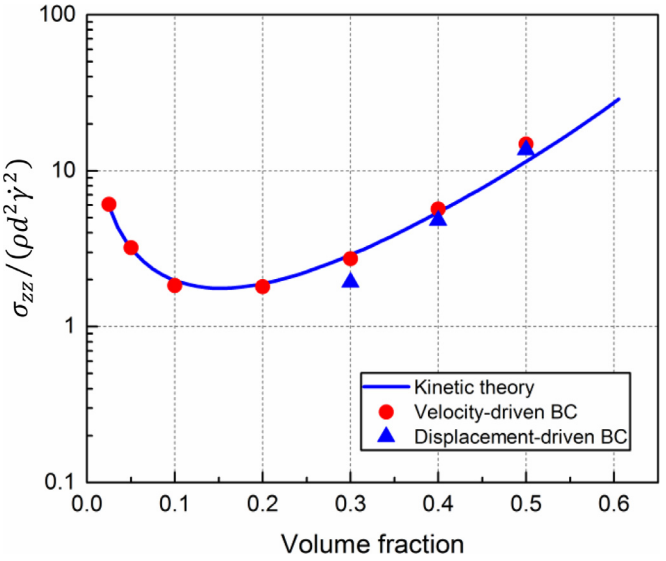

Fig. 23. Normalised normal stress as a function of volume fraction for the validation of the implementation of Lees-Edwards boundary.

Fig. 22 shows the resulting velocities of each particle when the particle stiffness is reduced. For the Hookean contact model, the velocity distribution of the stiffness of 500 N/m is similar to the original particle stiffness (7000 N/m); the identical particle velocities observed for particles 1–12, indicates that a large agglomerate of 12 particles, remains in both cases. However, a small quantitative difference is observable, the particle at the left side (particle 0) has a slightly smaller velocity in the case of 500 N/m. With further reduction in the particle stiffness, only 10 particles remain in an agglomerate. For the Hookean contact model, the performance of the present model is comparable to the study of Gu et al. [30]. For the Hertzian contact model, all the cases with scaled particle Young's modulus yield an agglomerate of 13 particles, even when the Young's modulus is reduced to 10^5 Pa (corresponding to a scaling ratio of 0.000143). Comparing with that of the Hookean contact model, the proposed force estimation method yields better prediction with the Hertzian contact model, indicating that the present DEM approach is also applicable for dilute fine particle systems, such as gas-solid fluidisation of Geldart's group A particles.

A.3. Validation of the implementation of Lees-Edwards boundary

Simulations of volume-controlled simple shear flow of inelastic spherical particles were conducted and compared with granular kinetic theory [48] to validate the implementation of Lees-Edwards boundary [45]. Fig. 23 plots the normal stress, normalised by $\rho d^2\dot{\gamma}^2$, as a function of the volume fraction. Modelling parameters are the same as that used in the study of Guo et al. [49]. Two types of the implementation are tested here. In the traditional implementation, particles' motion is driven by velocities as a result of interparticle forces while a displacement field according to the shearing profile is applied to drive particles in the approach proposed by Shi et al. [15]. The resulting particle velocity is thus the velocity fluctuation relative to its mean value in the displacement-driven approach. As shown in Fig. 23, the data predicted by the traditional velocity-driven implementation are in close agreement with that of the granular kinetic theory, especially at low volume fractions ($\leq$0.4). This is in consistent with the results obtained by Guo et al. [49]. The displacement-driven implementation shows good agreement with the traditional velocity-driven implementation, especially for higher volume fractions (i.e. $\geq$0.4). This shows that the displacement-driven implementation is better at predicting rheological behaviour of dense systems where multiple, enduring contacts dominates. Compared to the traditional velocity-driven implementation, the advantage of this approach is to ensure a homogeneous shearing which is critical for the simulations of cohesive particles and hence adopted in the present study.

References

[1] R.Y. Yang, R.P. Zou, A.B. Yu, Computer simulation of the packing of fine particles, Phys. Rev. E 62 (2000) 3900–3908, doi:10.1103/PhysRevE.62.3900.
[2] Y. He, Z. Wang, T.J. Evans, A.B. Yu, R.Y. Yang, DEM study of the mechanical strength of iron ore compacts, Int. J. Miner. Process. 142 (2015) 73–81, doi:10.1016/j.minpro.2015.05.005.
[3] Y. He, T.J. Evans, A.B. Yu, R.Y. Yang, DEM investigation of the role of friction in mechanical response of powder compact, Powder Technol. 319 (2017) 183–190, doi:10.1016/j.powtec.2017.06.055.
[4] Y. He, T.J. Evans, Y.S. Shen, A.B. Yu, R.Y. Yang, Discrete modelling of the compaction of non-spherical particles using a multi-sphere approach, Miner. Eng. 117 (2018) 108–116, doi:10.1016/j.mineng.2017.12.013.
[5] Y. He, Y.Y. Li, T.J. Evans, A.B. Yu, R.Y. Yang, Effects of particle characteristics and consolidation pressure on the compaction of non-spherical particles, Miner. Eng. 137 (2019) 241–249, doi:10.1016/j.mineng.2019.04.007.
[6] S.C. Thakur, H. Ahmadian, J. Sun, J.Y. Ooi, An experimental and numerical study of packing, compression, and caking behaviour of detergent powders, Particuology 12 (2014) 2–12, doi:10.1016/j.partic.2013.06.009.
[7] A.B. Yu, B.H. Xu, Particle-scale modelling of gas-solid flow in fluidisation, J. Chem. Technol. Biotechnol. 78 (2003) 111–121, doi:10.1002/jctb.788.
[8] S. Li, J.S. Marshall, G. Liu, Q. Yao, Adhesive particulate flow: the discrete-element method and its application in energy and environmental engineering, Prog. Energy Combust. Sci. 37 (2011) 633–668, doi:10.1016/j.pecs.2011.02.001.
[9] Q.F. Hou, K.J. Dong, A.B. Yu, DEM study of the flow of cohesive particles in a screw feeder, Powder Technol. 256 (2014) 529–539, doi:10.1016/j.powtec.2014.01.062.
[10] R. Schwarze, A. Gladkyy, F. Uhlig, Rheology of weakly wetted granular materials: a comparison of experimental and numerical data, Granul. Matter 15 (2013) 455–465, doi:10.1007/s10035-013-0430-z.
[11] H.C. Hamaker, The London-van der Waals attraction between spherical particles, Physica 4 (1937) 1058–1072, doi:10.1016/S0031-8914(37)80203-7.
[12] G. Lian, C. Thornton, M.J. Adams, A theoretical study of the liquid bridge forces between two rigid spherical bodies, J. Colloid Interface Sci. 161 (1993) 138–147, doi:10.1006/jcis.1993.1452.
[13] S. Matsusaka, H. Maruyama, T. Matsuyama, M. Ghadiri, Triboelectric charging of powders: a review, Chem. Eng. Sci. 65 (2010) 5781–5807, doi:10.1016/j.ces.2010.07.005.
[14] Y. Gu, S. Chialvo, S. Sundaresan, Rheology of cohesive granular materials across multiple dense-flow regimes, Phys. Rev. E 90 (2014) 032206, doi:10.1103/PhysRevE.90.032206.
[15] H. Shi, S. Roy, T. Weinhart, V. Magnanimo, S. Luding, Steady state rheology of homogeneous and inhomogeneous cohesive granular materials, Granul. Matter 22 (2020) 1–20, doi:10.1007/s10035-019-0968-5.
[16] S. Roy, A. Singh, S. Luding, T. Weinhart, Micro–macro transition and simplified contact models for wet granular materials, Comput. Part. Mech. 3 (2016) 449–462, doi:10.1007/s40571-015-0061-8.
[17] S. Roy, S. Luding, T. Weinhart, A general(ized) local rheology for wet granular materials, New J. Phys. 19 (2017) 043014, doi:10.1088/1367-2630/aa6141.
[18] M. Markl, K. Carolin, Multiscale modeling of powder bed – based additive manufacturing, Annu. Rev. Mater. Res. 46 (2016) 96–123, doi:10.1146/annurev-matsci-070115-032158.
[19] E.J.R. Parteli, T. Pöschel, Particle-based simulation of powder application in additive manufacturing, Powder Technol. 288 (2016) 96–102, doi:10.1016/j.powtec.2015.10.035.
[20] K.L. Johnson, K. Kendall, A.D. Roberts, Surface energy and the contact of elastic solids, Proc. R. Soc. Lond. A: Math. Phys. Sci. 324 (1971) 301–313, doi:10.1098/rspa.1971.0141.
[21] B.V. Derjaguin, V.M. Muller, Y.P. Toporov, Effect of contact deformation on the adhesion of particles, J. Colloid Interface Sci. 53 (1975) 314–326, doi:10.1016/0021-9797(75)90018-1.
[22] J. Yang, C. Wu, M. Adams, DEM analysis of the effect of particle-wall impact on the dispersion performance in carrier-based dry powder inhalers, Int. J. Pharm. 487 (2015) 32–38, doi:10.1016/j.ijpharm.2015.04.006.
[23] Y. He, F. Muller, A. Hassanpour, A.E. Bayly, A CPU-GPU cross-platform coupled CFD-DEM approach for complex particle-fluid flows, Chem. Eng. Sci. (2020) 115712, doi:10.1016/j.ces.2020.115712.
[24] Y. He, T.J. Evans, A.B. Yu, R.Y. Yang, A GPU-based DEM for modelling large scale powder compaction with wide size distributions, Powder Technol. 333 (2018) 219–228, doi:10.1016/j.powtec.2018.04.034.
[25] H. Mio, M. Akashi, A. Shimosaka, Y. Shirakawa, J. Hidaka, Speed-up of computing time for numerical analysis of particle charging process by using discrete element method, Chem. Eng. Sci. 64 (2009) 1019–1026, doi:10.1016/j.ces.2008.10.064.
[26] Y. Sheng, C.J. Lawrence, B.J. Briscoe, C. Thornton, Numerical studies of uniaxial powder compaction process by 3D DEM, Eng. Comput. 21 (2004) 304–317, doi:10.1108/02644400410519802.
[27] S.C. Thakur, J.Y. Ooi, H. Ahmadian, Scaling of discrete element model parameters for cohesionless and cohesive solid, Powder Technol. 293 (2016) 130–137, doi:10.1016/j.powtec.2015.05.051.
[28] S. Lommen, D. Schott, G. Lodewijks, DEM speedup: stiffness effects on behavior of bulk material, Particuology 12 (2014) 107–112, doi:10.1016/j.partic.2013.03.006.
[29] T. Kobayashi, T. Tanaka, N. Shimada, T. Kawaguchi, DEM-CFD analysis of fluidization behavior of Geldart Group A particles using a dynamic adhesion force model, Powder Technol. 248 (2013) 143–152, doi:10.1016/j.powtec.2013.02.028.

[30] Y. Gu, A. Ozel, S. Sundaresan, A modified cohesion model for CFD-DEM simulations of fluidization, Powder Technol. 296 (2016) 17–28, doi:10.1016/j.powtec.2015.09.037.
[31] K. Washino, E.L. Chan, T. Tanaka, DEM with attraction forces using reduced particle stiffness, Powder Technol. 325 (2018) 202–208, doi:10.1016/j.powtec.2017.11.024.
[32] S. Chen, W. Liu, S. Li, A fast adhesive discrete element method for random packings of fine particles, Chem. Eng. Sci. 193 (2019) 336–345, doi:10.1016/j.ces.2018.09.026.
[33] J. Hærvig, U. Kleinhans, C. Wieland, H. Spliethoff, A.L. Jensen, K. Sørensen, T.J. Condra, On the adhesive JKR contact and rolling models for reduced particle stiffness discrete element simulations, Powder Technol. 319 (2017) 472–482, doi:10.1016/j.powtec.2017.07.006.
[34] M. Alizadeh, M. Asachi, M. Ghadiri, A. Bayly, A. Hassanpour, A methodology for calibration of DEM input parameters in simulation of segregation of powder mixtures, a special focus on adhesion, Powder Technol. 339 (2018) 789–800, doi:10.1016/j.powtec.2018.08.028.
[35] E.J.R. Parteli, J. Schmidt, C. Blümel, K.E. Wirth, W. Peukert, T. Pöschel, Attractive particle interaction forces and packing density of fine glass powders, Sci. Rep. 4 (2014) 6227, doi:10.1038/srep06227.
[36] A. Gladkyy, R. Schwarze, Comparison of different capillary bridge models for application in the discrete element method, Granul. Matter 16 (2014) 911–920, doi:10.1007/s10035-014-0527-z.
[37] R.D. Mindlin, H. Deresiewicz, Elastic spheres in contact under varying oblique forces, ASME – J. Appl. Mech. 20 (1953) 327–344.
[38] P.W. Cleary, M.L. Sawley, DEM modelling of industrial granular flows: 3D case studies and the effect of particle shape on hopper discharge, Appl. Math. Model. 26 (2002) 89–111, doi:10.1016/S0307-904X(01)00050-6.
[39] A. Singh, V. Magnanimo, S. Luding, A Contact Model For Sticking of Adhesive Mesoscopic Particles, ArXiv Prepr. https://arxiv.org/abs/1503.03720v2 (2015).
[40] L. Aarons, S. Sundaresan, Shear flow of assemblies of cohesive and non-cohesive granular materials, Powder Technol. 169 (2006) 10–21, doi:10.1016/j.powtec.2006.07.013.
[41] R.Y. Yang, R.P. Zou, A.B. Yu, Voronoi tessellation of the packing of fine uniform spheres, Phys. Rev. E 65 (2002) 041302, doi:10.1103/PhysRevE.65.041302.
[42] X.L. Deng, N.D. Rajesh, Dynamic simulation of particle packing influenced by size, aspect ratio and surface energy, Granul. Matter 15 (2013) 401–415, doi:10.1007/s10035-013-0413-0.
[43] J. Yang, C.-Y. Wu, M. Adams, DEM analysis of particle adhesion during powder mixing for dry powder inhaler formulation development, Granul. Matter 15 (2013) 417–426, doi:10.1007/s10035-013-0405-0.
[44] A.B. Yu, J. Bridgwater, A. Burbidge, On the modelling of the packing of fine particles, Powder Technol. 92 (1997) 185–194, doi:10.1016/S0032-5910(97)03219-1.
[45] A.W. Lees, S.F. Edwards, The computer study of transport processes under extreme conditions, J. Phys. C Solid State Phys. 5 (1972) 1921–1929.
[46] S. Chialvo, J. Sun, S. Sundaresan, Bridging the rheology of granular flows in three regimes, Phys. Rev. E 85 (2012) 021305, doi:10.1103/PhysRevE.85.021305.
[47] P.G. Rognon, J.-N. Roux, M. Naaim, F. Chevoir, Dense flows of cohesive granular materials, J. Fluid Mech. 596 (2008) 21–47, doi:10.1017/S0022112007009329.
[48] C.K.K. Lun, S.B. Savage, D.J. Jeffrey, Kinetic theories for granular flow: inelastic particles in Couette flow and slightly inelastic particles in a general flowfield, J. Fluid Mech. 140 (1984) 223–256, doi:10.1017/S0022112084000586.
[49] Y. Guo, C. Wassgren, W. Ketterhagen, B. Hancock, B. James, J. Curtis, A numerical study of granular shear flows of rod-like particles using the discrete element method, J. Fluid Mech. 713 (2012) 1–26, doi:10.1017/jfm.2012.423.